ScienceDirect

Journal of Computational Physics

Volume 515, 15 October 2024, 113282

Reduced order modeling for a Schur complement method for fluid-structure interaction

Amy de Castro [1], Hyesuk Lee [2], Margaret M. Wiecek

Show more

https://doi.org/10.1016/j.jcp.2024.113282

Get rights and content

Highlights

- Extends a non-iterative Schur complement method for fluid-structure interaction.
- Couples a projection-based reduced order model with a reduced or full order model.
- Utilizes supremizer enrichment for velocity and displacement.
- Examines performance of coupled models with respect to errors, basis sizes, time.

Abstract

We present a non-iterative Schur complement method for the solution of a fluid-structure interaction problem, employing projection-based reduced order models (ROMs) on one or both subdomains. The formulation is strongly coupled, using a Lagrange multiplier to represent the interfacial stress, and solving a Schur complement equation allows for the independent solution of the subdomain equations at each time step. The inclusion of ROMs in this scheme provides a more robust framework and makes the technique more computationally appealing. Utilizing the supremizer enrichment technique, we offer detailed investigations into the performance of this method with respect to the use of supremizers and with respect to the basis sizes of the reduced order variables. Results indicate that the ROM-ROM coupled formulation yields results that agree well with the full order solution in a shorter computational time and with a large reduction in the size of the algebraic system.

Previous Next

MSC

65N30; 76M10; 74F10; 65N22

Keywords

Proper orthogonal decomposition (POD); Fluid-structure interaction; Supremizer enrichment; Schur complement method

1. Introduction

Fluid-structure interaction (FSI) problems often require solutions on highly refined meshes in order to obtain accurate results, which comes at a high computational cost in terms of storage and time. A common solution to this issue is the introduction of reduced order models (ROMs) into the framework. In multi-query contexts for design, shape, or parameter optimization or in applications requiring real time parameter estimation, reduced order modeling provides

invaluable speed-ups in computational time and reductions in system size. Successful application of ROMs to FSI problems includes areas such as aeroelastics [17], [36] and haemodynamics [13], [30].

The type of model order reduction we consider involves the development of a computational model of the original partial differential equation (PDE) system using a finite element or finite volume method, for example, and then simplifying the model by reducing the size of the resulting linear system.

In what follows, we refer to the reduced computational model as the reduced order model (ROM) and to the solution by the finite element method (FEM) of the FSI system as the full order model, although one could consider an alternate method to develop the full order model. We focus on projection-based methods for our ROMs, specifically proper orthogonal decomposition (POD)-Galerkin ROMs, as they tend to be commonly used in fluid and mechanical engineering applications.

1.1. Proper orthogonal decomposition

The POD method has been widely used in fluid mechanics problems [2], [3], [5], [6], [23], [50] since its introduction by Lumley [37], producing a set of basis functions which are optimal in terms of energy decomposition. Particularly, POD is employed to develop bases for time-dependent problems, while greedy reduced basis methods are often applied for parameter-dependent problems [31], [45]. In POD, the original variables of the FEM system, which may have an intractably large number of degrees of freedom (DoFs) for a realistic computation, are represented by a small number of dominant global modes that retain most of the energy present in the original unknowns. This is accomplished through a spectral decomposition, extracting eigenvectors or singular vectors of a particular full order representation of the original state variables that correspond to dominant eigenvalues or singular values. Most often, the POD basis functions are obtained by using the method of snapshots [50], as extracting eigenmodes directly from the PDE system itself is expensive [35]. The eigenvalues or singular values must decay rapidly enough so that the main behavior of the system may be represented by retention of the dominant modes. For example, advection-dominated problems experience slow decay of singular values, as represented by the Kolmogorov n-width; these problems require extra pre-processing steps or the use of an alternative method to POD [42], [31]. Examination of these types of problems is beyond the scope of this paper. For in depth explanations of POD and its mathematical properties, see [8], [9], [11], [35], [45], [46].

1.2. Application of reduced order models to fluid problems

In extending the Schur complement coupling technique for FSI problems, presented in [16], to include a reduced order model on one or both subdomains, the main issues that arise will be on the fluid side. Thus, we first review existing techniques and best practices for applying ROMs to fluid problems. One of the foremost concerns for ROMs in a fluid context is pressure stability, as it may not be guaranteed in the reduced system even if the original FEM spaces and formulation satisfy inf-sup stability properties.

Frequently when implementing a POD ROM for an incompressible fluid, the pressure variable is dropped; as the problem data used to produce the ROM is discretely divergence-free, the reduced velocity space also enjoys divergence-free properties, negating the need for the pressure variable [11], [31].

If the pressure is not included in the ROM but is needed for later calculations or results, it can be recovered by solving a pressure Poisson equation, which requires an appropriate Neumann boundary condition, or by solving the original momentum equation using a supremizer enrichment technique [28]. Overall, the latter seems to enjoy a higher accuracy and does not require additional boundary conditions, but its reliability is subject to an appropriate inf-sup condition and other information relating to the velocity and supremizer spaces [28]. See [28] for stability and error analyses of these approaches.

However, the need for pressure in physical simulations and applications, the inclusion of pressure in some boundary conditions, and the possible loss of discrete divergence-free properties in certain discretizations of the fluid equations suggest that retaining the pressure in the reduced formulation may be necessary and often can provide better solutions [11]. Additionally, the use of Galerkin projection does not guarantee the fulfillment of the reduced inf-sup condition [2].

For these reasons, we choose to retain the pressure in our formulation and briefly survey a few common techniques used by others to address a stable approximation of the pressure. These include the application of a stabilized projection method such as Chorin-Temam [34], [40], the addition of extra stabilization terms into the formulation (such as [49] for Local Projection Stabilization, [27] for Ghost Penalty stabilization, [2] for pressure-Poisson stabilized Galerkin, [53] for variational multiscale), or the supremizer enrichment technique [40]. Additional investigations into the stability of ROMs for Navier-Stokes equations (NSE) may be found in [1], [24].

We utilize the supremizer enrichment technique, as it is heavily used in ROMs for fluids, does not require inserting additional terms for stability into the weak form, and is more flexible in terms of geometric variation in the domain [5]. The exact supremizer method uses pressure basis functions to compute supremizer functions which are guaranteed to satisfy inf-sup conditions, while the approximate supremizer method uses pressure snapshots, obtained from solving a FEM, to compute similar functions [25]. The approximate method is almost exclusively utilized in practice, but stability properties can only be rigorously proven for the exact supremizer method [5], [25]. For problems which are not parameter dependent, using the approximate method to calculate the supremizers once during the offline stage produces acceptable results; more care should be taken with parameter dependent problems [28]. Bounds on the inf-sup constant with supremizers may be proven for parameter dependent problems, as seen in [38], [48], [47].

The following references provide a more detailed investigation into supremizer enrichment: parameterized Stokes [38], [47], parameterized steady and unsteady NSE [18], [27], [38], pressure recovery formulations [28], monolithic FSI formulations [6], [40], inverse problems for FSI [30], [48], and alternate formulations and orthonormalization techniques [48]. In the context of domain decomposition for the NSE, [44] presented initial comparisons between ROM and FEM couplings with respect to performance and accuracy.

In this paper, we choose to compute separate POD modes for the pressure, following work such as [7], [25]; alternative formulations utilize the velocity POD modes to compute a ROM for the pressure [19], [39]. Caiazzo et al. offer a comparison of these types of formulations [11].

Several works provide helpful examinations of the properties and performance of formulations that stabilize offline and online calculations and/or include supremizer enrichment. Ali et al. find that stabilization in both the offline and online phases is most important for FE spaces for Stokes and NSE which are not inf-sup compliant, such as $\mathscr{P}_k/\mathscr{P}_k$, while for $\mathscr{P}_2/\mathscr{P}_1$, supremizers improve the accuracy of the pressure approximation [2], [3]. Stabile et al. provide a comparison between a supremizer enrichment and a pressure Poisson equation method to stabilize the pressure approximation in the NSE, finding that the supremizer approach may suffer from numerical instabilities over long time integration scales [52].

1.3. Application of reduced order models to FSI systems

We briefly review existing methods and results for applying ROMs in the context of FSI.

The Chorin-Temam projection scheme, developed by Chorin and Temam in 1968 for fluid

problems [12], [21], [54], is a semi-implicit scheme which allows the discrete velocity and pressure spaces not to satisfy the inf-sup condition [34], [40]. However, Guermond et al. find scenarios in which Chorin-Temam schemes have a stability dependent on the time step Δt, allowing spurious pressure modes to arise if Δt becomes too small [20]. The Chorin-Temam scheme has been extended to FSI problems using a Robin-Neumann coupling condition in works such as [7], [40], [41]. It requires an explicit step to compute fluid velocity and an implicit step to compute fluid pressure and structural displacement which iterates until convergence. For an alternative approach to implicitly coupled FSI problems with black box fluid and structural solvers, see [55].

In contrast, the scheme presented in this paper requires no iterations between subproblems; it is "one-shot" in the sense that once the Schur complement equation is solved for the Lagrange multiplier (LM) and pressure, each of the fluid and structure subdomain problems may be updated separately at each time step.

Previous works for ROMs for FSI problems include applications such as investigation of a haemodynamics problem using a reduced version of the PDE system [13], reduced modeling of an aircraft configuration by interpolating the angle between two POD subspaces for different Mach numbers [36], an inverse FSI problem [30], and a stabilized formulation in the case of a linearized compressible inviscid flow and a flat linear von Kármán plate [26]. Additional works include an investigation into three different ROM formulations without supremizers [11], a monolithic scheme employing a LM [40], a fictitious domain approach [35], parametric coupling utilizing the steady Stokes equations [32], Chorin-Temam schemes [7], [40], [41], and a FETI-local method with additional penalty weight added [33]. In the latter, domain decomposition is used as a tool to facilitate parallel computation.

For our ROM development, we retain the pressure variable in our formulation and calculate separate POD modes, choosing to address the instability issues through supremizer enrichment. We investigate the unsteady Stokes equations coupled with the linear elasticity equations using a partitioned approach. Our coupling scheme differs from the other FSI ROM works listed above, as we follow the Lagrange multiplier technique for FSI problems outlined in [16], which is based on the Schur complement approach of [43], [51]. Our formulation is strongly coupled, as a precise expression of the LM is calculated using a Schur complement equation and then passed to each subdomain solver, instead of requiring iterations between subdomains to establish interface boundary conditions.

For some iterative methods, one has to serially compute the solutions for each subdomain and

iterate between the subdomains to solve for the interface condition at each time step. The Schur complement method, on the other hand, allows for parallel computation of the subproblems at each time step as the Schur complement equation provides a “one-shot” solution to the interface boundary condition. We expect that the advantages of parallel computation of decoupled subproblems and a non-iterative solve for the interface boundary condition will prove beneficial in general, provided the Schur complement equation is equipped with an appropriate preconditioner. Additionally, the use of strongly coupled subproblems generally has better stability properties, which is useful when solving problems plagued by the added mass effect. See [14], [16] for more details. The main contribution of this work is the extension of the partitioned coupling scheme in [16], which requires no subdomain iterations, to the more robust framework of coupling a ROM on one subdomain to a ROM or a FEM on another subdomain. We demonstrate this method's performance by showing its ability to obtain solutions as accurate as the FEM-FEM coupling with reduced expenses in computational time.

The rest of the paper is constructed as follows. In Section 2, we give the model equations and weak form, followed by a brief review of the partitioned method in the case of a FEM-FEM coupling in Section 3. Section 4 overviews our POD-Galerkin strategy for ROM development, as well as the formulation of the supremizer functions utilized. We combine this ROM model with the coupling scheme to obtain the ROM-ROM coupling formulation in Section 5. We note that our formulation applies in a straightforward fashion to the coupling of a FEM with a ROM as well, but for the sake of brevity we omit that formulation in this paper. However, a FEM-ROM coupling may be desirable in some applications [14], [15], [44]. Lastly, we present and discuss numerical results which confirm the method's accuracy and efficiency in Section 6, followed by our conclusions and ideas for extensions of this work in Section 7.

2. Model equations

In this section, we provide the strong and weak form of our FSI model equations, coupling a linear elastic structure to an incompressible Newtonian fluid. We make two simplifications to ease the development of the partitioned method, focusing on the linear Stokes equations in the context of a fixed domain. Extensions to nonlinearity and moving domains may be considered in future work.

For $d = 2, 3$, let $\Omega_f, \Omega_s \in \mathbb{R}^d$ refer to the physical fluid and structure domains with Lipschitz continuous boundaries, respectively. The interface between the non-overlapping subdomains is denoted by γ. With subscripts “N” and “D” referencing portions of the boundary on which

Neumann and Dirichlet boundary conditions are prescribed, domain boundaries are denoted by Γ^f, Γ^s, where $\Gamma^f = \Gamma^f_N \cup \Gamma^f_D \cup \gamma$ and $\Gamma^s = \Gamma^s_N \cup \Gamma^s_D \cup \gamma$. We assume the measure of Γ^k_N and Γ^k_D is nonzero on both domains Ω_k and denote outward normal vectors to Ω_k by $\boldsymbol{n_k}$, for $k \in \{f, s\}$. Let T denote a given final time and denote the temporal domain by $(0, T]$.

The following spaces are needed for the formulation. Let $L^2(\Omega_k)$ $\left(\text{or, } L^2(\Gamma^k)\right)$ denote the space of square integrable functions on Ω_k $\left(\text{or, } \Gamma^k\right)$, with inner product and norm denoted by $(\cdot,\cdot)_{\Omega_k}$, and $||\cdot||_{\Omega_k}$ $(\text{or, } (\cdot,\cdot)_{\Gamma^k}$ and $||\cdot||_{\Gamma^k})$. Likewise, $H^1(\Omega_k)$ is the space of functions in $L^2(\Omega_k)$ whose gradients are also square integrable. Duality pairings between $H^{-1}(\omega)$ and $H^1(\omega)$ or $H^{-1/2}(\omega)$ and $H^{1/2}(\omega)$, for a subdomain or interface ω, are denoted by $\langle\cdot,\cdot\rangle_\omega$.

The three unknowns in our FSI system are the fluid velocity $\boldsymbol{u}(\boldsymbol{x}, t)$, fluid pressure $p(\boldsymbol{x}, t)$, and structural displacement $\boldsymbol{\eta}(\boldsymbol{x}, t)$. Body forces $\boldsymbol{f_f}, \boldsymbol{f_s}$ and Neumann conditions $\boldsymbol{u_N}, \boldsymbol{\eta_N}$ are provided for each subdomain, as well as positive constants $\rho_f, \rho_s, \nu_f, \nu_s, \lambda$, representing fluid density, structural density, fluid viscosity, and the Lamé parameters. Denoting the rate of strain tensor by $D(\boldsymbol{v}) := \frac{1}{2}(\nabla \boldsymbol{v} + (\nabla \boldsymbol{v})^T)$, the continuous FSI system may be posed as follows.

Find $\boldsymbol{u} \in \Omega_f \times (0, T] \mapsto \mathbb{R}^d$, $p \in \Omega_f \times (0, T] \mapsto \mathbb{R}$, $\boldsymbol{\eta} \in \Omega_s \times (0, T] \mapsto \mathbb{R}^d$ *such that*

$$\rho_f \frac{\partial \boldsymbol{u}}{\partial t} - 2\nu_f \nabla \cdot D(\boldsymbol{u}) + \nabla p = \boldsymbol{f_f} \quad \text{in } \Omega_f \times (0, T], \tag{2.1}$$

$$\nabla \cdot \boldsymbol{u} = 0 \quad \text{in } \Omega_f \times (0, T], \tag{2.2}$$

$$\rho_s \frac{\partial^2 \boldsymbol{\eta}}{\partial t^2} - 2\nu_s \nabla \cdot D(\boldsymbol{\eta}) - \lambda \nabla(\nabla \cdot \boldsymbol{\eta}) = \boldsymbol{f_s} \quad \text{in } \Omega_s \times (0, T]. \tag{2.3}$$

We provide appropriate initial conditions, as well as both Dirichlet and Neumann boundary conditions

$$\begin{aligned} (2\nu_f D(\boldsymbol{u}) - pI)\boldsymbol{n_f} &= \boldsymbol{u_N} \quad \text{on } \Gamma^f_N \times (0, T], \qquad \boldsymbol{u} = \boldsymbol{0} \quad \text{on } \Gamma^f_D \times (0, T], \\ (2\nu_s D(\boldsymbol{\eta}) + \lambda(\nabla \cdot \boldsymbol{\eta})I)\boldsymbol{n_s} &= \boldsymbol{\eta_N} \quad \text{on } \Gamma^s_N \times (0, T], \qquad \boldsymbol{\eta} = \boldsymbol{0} \quad \text{on } \Gamma^s_D \times (0, T]. \end{aligned} \tag{2.4}$$

The two interface conditions on γ enforce the continuity of velocity and the continuity of stress force,

$$\frac{\partial \boldsymbol{\eta}}{\partial t} = \boldsymbol{u} \quad \text{on } \gamma \times (0, T], \tag{2.5}$$

$$(2\nu_f D(\boldsymbol{u}) - pI)\boldsymbol{n_f} = -(2\nu_s D(\boldsymbol{\eta}) + \lambda(\nabla \cdot \boldsymbol{\eta})I)\boldsymbol{n_s} \quad \text{on } \gamma \times (0, T]. \tag{2.6}$$

Define the following function spaces for velocity, pressure, and displacement:

$$U := \{\boldsymbol{v} \in \boldsymbol{H}^1(\Omega_f) : \boldsymbol{v} = \boldsymbol{0} \text{ on } \Gamma_D^f\}, \quad Q := L^2(\Omega_f), \quad X := \{\boldsymbol{\varphi} \in \boldsymbol{H}^1(\Omega_s) : \boldsymbol{\varphi} = \boldsymbol{0} \text{ on } \Gamma_D^s\}. \tag{2.7}$$

We enforce the continuity of velocity equation (2.5) as a constraint in the system using a Lagrange multiplier (LM) in $\Lambda := H^{-1/2}(\gamma)$, which yields the following weak form.

Find $\boldsymbol{u} \in U, p \in Q, \boldsymbol{\eta} \in X, \boldsymbol{g} \in \Lambda$ *such that*

$$\begin{aligned} &\rho_f \left(\frac{\partial \boldsymbol{u}}{\partial t}, \boldsymbol{v}\right)_{\Omega_f} + 2\nu_f (D(\boldsymbol{u}), D(\boldsymbol{v}))_{\Omega_f} - (p, \nabla \cdot \boldsymbol{v})_{\Omega_f} - \langle \boldsymbol{g}, \boldsymbol{v} \rangle_\gamma = \langle \boldsymbol{f_f}, \boldsymbol{v} \rangle_{\Omega_f} \\ &+ \langle \boldsymbol{u}_N, \boldsymbol{v} \rangle_{\Gamma_N^f} \quad \forall \boldsymbol{v} \in U, \\ &\qquad\qquad (\nabla \cdot \boldsymbol{u}, q)_{\Omega_f} = 0 \quad \forall q \in Q, \\ &\rho_s \left(\frac{\partial^2 \boldsymbol{\eta}}{\partial t^2}, \boldsymbol{\varphi}\right)_{\Omega_s} + 2\nu_s (D(\boldsymbol{\eta}), D(\boldsymbol{\varphi}))_{\Omega_s} + \lambda (\nabla \cdot \boldsymbol{\eta}, \nabla \cdot \boldsymbol{\varphi})_{\Omega_s} + \langle \boldsymbol{g}, \boldsymbol{\varphi} \rangle_\gamma = \langle \boldsymbol{f_s}, \boldsymbol{\varphi} \rangle_{\Omega_s} \\ &+ \langle \boldsymbol{\eta}_N, \boldsymbol{\varphi} \rangle_{\Gamma_N^s} \quad \forall \boldsymbol{\varphi} \in X, \\ &\qquad\qquad \left\langle \frac{\partial \boldsymbol{\eta}}{\partial t}, \boldsymbol{s} \right\rangle_\gamma - \langle \boldsymbol{u}, \boldsymbol{s} \rangle_\gamma = 0 \quad \forall \boldsymbol{s} \in \Lambda. \end{aligned} \tag{2.8}$$

We observe that the LM $\boldsymbol{g}$ represents the interface stress force (2.6); namely, on γ, $\boldsymbol{g} = (2\nu_f D(\boldsymbol{u}) - pI)\boldsymbol{n_f} = -(2\nu_s D(\boldsymbol{\eta}) + \lambda(\nabla \cdot \boldsymbol{\eta})I)\boldsymbol{n_s}$. It can be shown that the semi-discrete saddle point problem arising from this weak form is well-posed [16].

3. Partitioned method for FEM-FEM coupling

In this section, we briefly review the fully discretized formulation of the FEM and our partitioned scheme for the FEM-FEM coupling. More details and analysis may be found in [16]. We use standard discrete FEM spaces for $\boldsymbol{u}, p, \boldsymbol{\eta}, \boldsymbol{g}$, noting that the LM subspace Λ^h used is a subspace of $\boldsymbol{H}^{1/2}(\gamma)$ as higher regularity is needed for well-posedness of the fully discrete formulation.

Discretizing (2.8) in time with first order approximations and posing it over the finite element spaces results in a linear system.

(3.1)

$$M_f \boldsymbol{u}^{n+1} + \Delta t K_f \boldsymbol{u}^{n+1} - \Delta t P \boldsymbol{p}^{n+1} - \Delta t G_f^T \boldsymbol{g}^{n+1} = \Delta t \overline{\boldsymbol{f}}_{\boldsymbol{f}}{}^{n+1} + M_f \boldsymbol{u}^n,$$
$$P^T \boldsymbol{u}^{n+1} = \boldsymbol{0},$$
$$\frac{1}{\Delta t} M_s \boldsymbol{\eta}^{n+1} + \Delta t (K_s + L) \boldsymbol{\eta}^{n+1} + \Delta t G_s^T \boldsymbol{g}^{n+1} = \Delta t \overline{\boldsymbol{f}}_{\boldsymbol{s}}{}^{n+1} + \frac{2}{\Delta t} M_s \boldsymbol{\eta}^n - \frac{1}{\Delta t} M_s \boldsymbol{\eta}^{n-1},$$
$$\frac{1}{\Delta t} G_s \boldsymbol{\eta}^{n+1} - G_f \boldsymbol{u}^{n+1} = \frac{1}{\Delta t} G_s \boldsymbol{\eta}^n.$$

Above, mass and stiffness matrices are given by M_k, K_k, and $\overline{\boldsymbol{f}}_{\boldsymbol{k}}$ holds both the body forces and Neumann boundary terms for $k \in \{f, s\}$. Pressure and divergence terms are encapsulated in P and L, and the G matrices represent the interaction between the interface and subdomain bases, where $\{v_i\}, \{\varphi_i\}$, and $\{\mu_i\}$ are the FEM scalar basis functions for the full order velocity, displacement, and LM spaces, respectively. Then G_f, G_s have a block diagonal structure due to our ordering of the DoFs: for $d = 2$,

$$G_f = \begin{bmatrix} G_f^1 & 0 \\ 0 & G_f^2 \end{bmatrix}, \quad \text{with } \left(G_f^r\right)_{i,j} = \langle v_j, \mu_i \rangle_\gamma \text{ for } r = 1, 2$$
$$G_s = \begin{bmatrix} G_s^1 & 0 \\ 0 & G_s^2 \end{bmatrix}, \quad \text{with } \left(G_s^r\right)_{i,j} = \langle \varphi_j, \mu_i \rangle_\gamma \text{ for } r = 1, 2.$$

The saddle point system associated with this linear system is also well-posed, see [16] for details. Our formulation requires grouping the pressure with the LM and appropriately blocking the equations of (3.1). With

$$\boldsymbol{z}^{n+1} := \begin{bmatrix} \boldsymbol{p}^{n+1} \\ \boldsymbol{g}^{n+1} \end{bmatrix}, \; A_f := \begin{bmatrix} P^T \\ G_f \end{bmatrix}, \; A_s := \begin{bmatrix} 0 \\ G_s \end{bmatrix}, \; \widetilde{\boldsymbol{\eta}}^{n+1} := \tfrac{1}{\Delta t} \boldsymbol{\eta}^{n+1}, \text{ and } \tilde{\boldsymbol{z}}^{n+1} := \Delta t \boldsymbol{z}^{n+1}$$

we obtain

$$\begin{aligned} W_f \boldsymbol{u}^{n+1} - A_f^T \tilde{\boldsymbol{z}}^{n+1} &= \boldsymbol{w_1}^n, \\ W_s \widetilde{\boldsymbol{\eta}}^{n+1} + A_s^T \tilde{\boldsymbol{z}}^{n+1} &= \boldsymbol{w_2}^n, \\ A_s \widetilde{\boldsymbol{\eta}}^{n+1} - A_f \boldsymbol{u}^{n+1} &= \boldsymbol{w_3}^n, \end{aligned} \tag{3.2}$$

where

$$W_f := M_f + \Delta t K_f, \qquad W_s := M_s + \Delta t^2 (K_s + L),$$
$$\boldsymbol{w_1}^n := \Delta t \overline{\boldsymbol{f}}_{\boldsymbol{f}}{}^{n+1} + M_f \boldsymbol{u}^n, \qquad \boldsymbol{w_2}^n := \Delta t \overline{\boldsymbol{f}}_{\boldsymbol{s}}{}^{n+1} + \tfrac{2}{\Delta t} M_s \boldsymbol{\eta}^n - \tfrac{1}{\Delta t} M_s \boldsymbol{\eta}^{n-1}, \quad \boldsymbol{w_3}^n := \begin{bmatrix} 0 \\ \frac{1}{\Delta t} G_s \boldsymbol{\eta}^n \end{bmatrix}.$$

Solving the first two equations of (3.2) for $\boldsymbol{u}^{n+1}$ and $\widetilde{\boldsymbol{\eta}}^{n+1}$ and substituting into the constraint equation of (3.2) yields

$$\left(A_f W_f^{-1} A_f^T + A_s W_s^{-1} A_s^T \right) \tilde{\boldsymbol{z}}^{n+1} = A_s W_s^{-1} \boldsymbol{w_2}^n - A_f W_f^{-1} \boldsymbol{w_1}^n - \boldsymbol{w_3}^n. \tag{3.3}$$

Equation (3.3), the Schur complement equation, is at the center of our method. Letting S be the matrix on the left hand side, we can solve (3.3) for $\tilde{\boldsymbol{z}}^{n+1}$ once at each time step when S is full rank. Plugging $\tilde{\boldsymbol{z}}^{n+1}$ back in to the first two equations of (3.2) effectively decouples the system and allows for the independent solution of $\boldsymbol{u}^{n+1}$ and $\widetilde{\boldsymbol{\eta}}^{n+1}$.

As a motivation for the use of reduced order modeling, consider the matrix sizes involved in the Schur complement equation and subdomain solves. Denote by $N_u, N_p, N_\eta,$ and N_g the total number of DoFs for each variable. Then the matrices W_f, W_s are of size $N_u \times N_u$ and $N_\eta \times N_\eta$, respectively, and the constraint matrices A_f, A_s have dimension $(N_p + N_g) \times N_u$ and $(N_p + N_g) \times N_\eta$. Thus, S is a $(N_p + N_g) \times (N_p + N_g)$ matrix. For high-fidelity FEM computations, the number of DoFs may become intractably large for solving these linear systems. ROMs present a solution to this issue by retaining only dominant modes of the system, allowing a significant size reduction in the linear system and thereby computational speedups as well.

4. ROM construction and implementation

We utilize a projection based reduced order model, using a technique known as proper orthogonal decomposition (POD) to create the reduced basis. Before presenting our coupled reduced order models for the FSI system, we begin with a brief discussion on how to construct this projection-based ROM in two stages: POD and Galerkin projection [23], [50].

4.1. General setting: POD and Galerkin projection

Consider a generic full order model, expressed by $A\dot{\boldsymbol{u}} = \boldsymbol{f}(\boldsymbol{u})$, with $A \in \mathbb{R}^{\ell \times \ell}$ and $\boldsymbol{u}, \boldsymbol{f} \in \mathbb{R}^\ell$. In the method of snapshots, a high-fidelity full order model is solved over a collection of times and/or parameter values. The solution vectors $\boldsymbol{u}^j$ for $j = 1, \ldots, m$ are arranged as columns of a

matrix $\boldsymbol{X} \in \mathbb{R}^{\ell \times m}$, referred to as the snapshot matrix. In general, we assume $m < \ell$. We compute the singular value decomposition (SVD) of the snapshot matrix, $\boldsymbol{X} = U\Sigma V^T$. For our formulation, we follow the approach in [22] and only calculate the SVD on the rows of *X* corresponding to non-Dirichlet nodes, padding the output matrix *U* with zeros in Dirichlet rows.

The reduced basis space is then defined by the first *r* columns of *U*, for $r \ll m$. The number of columns retained is determined by an energy criterion: we choose a δ such that $1 - \delta$ is the desired proportion of the snapshot energy captured in the basis. We then solve for the smallest number of columns *r* that satisfies the equation

$$1 - \delta \leq \frac{\sum_{i=1}^{r} \sigma_i^2}{\sum_{i=1}^{m} \sigma_i^2}. \tag{4.1}$$

We refer to the matrix $\widetilde{\boldsymbol{\Phi}} \in \mathbb{R}^{\ell \times r}$, containing the first *r* columns of U, as the reduced basis matrix. The columns of $\widetilde{\boldsymbol{\Phi}}$, known as the POD modes, are spatially and temporally independent, orthogonal, and globally defined, instead of locally defined as with traditional FEM basis functions.

For this method to be effective, the *r* dominant singular values corresponding to the first *r* left singular vectors are assumed to contain most of the energy of the system. POD may not be the method of choice when the energy decays slowly, but work has been done to make POD more robust in these cases [31], [42].

We may consider the more general case of non-homogeneous Dirichlet boundaries, by defining a vector $\boldsymbol{\beta_R} \in \mathbb{R}^{\ell}$ that contains the Dirichlet boundary information at appropriate nodes and is zero elsewhere. Once the reduced basis matrix $\widetilde{\boldsymbol{\Phi}}$ is constructed, we use the ansatz $\boldsymbol{u} = \widetilde{\boldsymbol{\Phi}}\boldsymbol{u_R} + \boldsymbol{\beta_R}$, where $\boldsymbol{u} \in \mathbb{R}^{\ell}$ is the full order variable and $\boldsymbol{u_R} \in \mathbb{R}^{r}$ is the reduced order variable. Recall that $\widetilde{\boldsymbol{\Phi}}$ contains zeros on each Dirichlet row, so that $\widetilde{\boldsymbol{\Phi}}\boldsymbol{u_R}$ is zero at each row corresponding to a Dirichlet node. Substituting this expression into $A\dot{\boldsymbol{u}} = \boldsymbol{f}(\boldsymbol{u})$, multiplication by $\widetilde{\boldsymbol{\Phi}}^T$ projects the equations into the reduced-dimensional space, yielding the reduced system

$$\widetilde{\boldsymbol{\Phi}}^T A(\widetilde{\boldsymbol{\Phi}}\dot{\boldsymbol{u}}_{\boldsymbol{R}} + \dot{\boldsymbol{\beta}}_{\boldsymbol{R}}) = \widetilde{\boldsymbol{\Phi}}^T \boldsymbol{f}(\widetilde{\boldsymbol{\Phi}}\boldsymbol{u_R} + \boldsymbol{\beta_R}).$$

4.2. Supremizer enrichment: inf-sup stability

Stability of our coupled problem in its reduced formulation, and in particular the fluid portion, is a necessary component. For the reduced order formulation, the LBB condition satisfied by the full order spaces is not guaranteed to be satisfied by the Galerkin projection onto the reduced spaces.

The following technique is employed to address the issue of instabilities due to violations of the discrete inf-sup condition.

Following works such as [2], [5], [6], [25], [40], [47], [48], we use the approximate supremizer enrichment method. As our problem is time dependent, and varying the parameters is not considered, the approximate method allows us to calculate the supremizer basis functions once during the offline stage at lower cost and also provides more variability in picking the size of the supremizer basis. Although this method does not allow us to rigorously prove inf-sup stability (see [5]), we will provide an examination of the performance of formulations with and without supremizers in the numerical results section and observe that the approximate supremizer method provides the needed stabilization for our problems.

The approximate supremizer method employs snapshots for the pressure and LM terms to create supremizer functions for the velocity and displacement that can be added into the velocity and displacement spaces to enrich them. Specifically, using the snapshots $\boldsymbol{p}(t^j), \boldsymbol{g}(t^j)$ collected for the pressure and Lagrange multipliers during the m time steps of the offline stage, the supremizer functions $\boldsymbol{s_u}(t^j), \boldsymbol{s_\eta}(t^j)$ are defined as [5]:

$$\begin{bmatrix} K_f & 0 \\ 0 & K_s \end{bmatrix} \begin{bmatrix} \boldsymbol{s_u}(t^j) \\ \boldsymbol{s_\eta}(t^j) \end{bmatrix} = \begin{bmatrix} P & G_f^T \\ 0 & G_s^T \end{bmatrix} \begin{bmatrix} \boldsymbol{p}(t^j) \\ \boldsymbol{g}(t^j) \end{bmatrix} \tag{4.2}$$

For each snapshot, we solve (4.2) to create velocity and displacement supremizer functions. Of course, (4.2) may be decoupled to solve for the velocity and displacement supremizer functions separately. Once the functions $\boldsymbol{s_u}(t^j), \boldsymbol{s_\eta}(t^j)$ are obtained, they are added as basis functions into the velocity and displacement spaces and orthogonalized against the existing POD basis functions. If $\{\Phi_u^1, \Phi_u^2, \dots, \Phi_u^r\}$ are the POD basis functions for velocity, then the set $\{\Phi_u^1, \dots, \Phi_u^r, \boldsymbol{s_u}(t^1), \dots, \boldsymbol{s_u}(t^m)\}$ represents the basis space with supremizers added, and we then perform modified Gram-Schmidt orthogonalization on this set of vectors to create the final reduced basis.

5. ROM-ROM coupling

We now derive a system similar to (3.2) for a coupled ROM-ROM instead of FEM-FEM. First, consider implementing a reduced order model on $\boldsymbol{\Omega_s}$. Using the process described in Section 4.1, we construct a reduced order basis matrix $\widetilde{\boldsymbol{\Phi}}_\eta$ such that the FEM coefficients for the displacement variable, $\boldsymbol{\eta}$, may be expressed as: $\boldsymbol{\eta}(t) = \widetilde{\boldsymbol{\Phi}}_\eta \boldsymbol{\eta_R}(t) + \boldsymbol{\beta}_\eta(t)$, where $\boldsymbol{\eta_R}(t) \in \mathbb{R}^{N_{R,\eta}}$ is the reduced time-dependent vector of solution coefficients for the displacement and

$\boldsymbol{\beta}_\eta(t) \in \mathbb{R}^{N_\eta}$ contains the possibly time-dependent Dirichlet boundary values in rows corresponding to Dirichlet nodes, and zeroes elsewhere. Snapshots may be constructed by solving the coupled FEM-FEM problem over Ω_s and Ω_f or only solving the structural problem on Ω_s, which requires providing a guess for the boundary conditions on γ.

The matrix $\widetilde{\boldsymbol{\Phi}}_\eta$ is of dimension $N_\eta \times N_{R,\eta}$, where $N_{R,\eta} \ll N_\eta$. Once the final solution $\boldsymbol{\eta_R}$ is obtained, we may recover the full order solution $\boldsymbol{\eta}$ by computing $\boldsymbol{\eta} = \widetilde{\boldsymbol{\Phi}}_\eta \boldsymbol{\eta_R} + \boldsymbol{\beta}_\eta$. Likewise, we may develop a reduced order basis for the velocity and pressure $\boldsymbol{u}, \boldsymbol{p} \in \Omega_f$ and express the full order coefficients as $\boldsymbol{u}(t) = \widetilde{\boldsymbol{\Phi}}_u \boldsymbol{u_R}(t) + \boldsymbol{\beta}_u(t), \text{ and } \boldsymbol{p}(t) = \widetilde{\boldsymbol{\Phi}}_p \boldsymbol{p_R}(t)$. Note that the ansatz for the pressure does not include a vector $\boldsymbol{\beta}_p$ for boundary information, as Dirichlet boundary conditions are only provided for displacement and velocity.

For our formulation, we also must reduce the LM, as it is coupled with the pressure and will overconstrain the problem if left at its full size. To this end we develop a POD basis, encapsulated in $\widetilde{\boldsymbol{\Phi}}_g$, to express the LM as $\boldsymbol{g}(t) = \widetilde{\boldsymbol{\Phi}}_g \boldsymbol{g_R}(t)$. We choose to collect snapshots of the LM term and conduct POD on them separately. Note that we solve the coupled formulation in the offline stage, which produces the LM as a variable at each time step. If a different offline procedure was used that did not solve for the LM explicitly, snapshots could be constructed from a combination of the velocity and pressure snapshots or from the displacement snapshots.

In formulations that include supremizers, we solve (4.2) for $\boldsymbol{s_u}(t^j), \boldsymbol{s_\eta}(t^j)$ for each time step t^j, $j = 1, \ldots, m$, and add these into the existing basis $\widetilde{\boldsymbol{\Phi}}_u$ and $\widetilde{\boldsymbol{\Phi}}_\eta$, re-orthogonalizing to get the new basis. With a slight abuse of notation, we let $\widetilde{\boldsymbol{\Phi}}_u, \widetilde{\boldsymbol{\Phi}}_\eta$ refer to the entire reduced basis in either scenario with or without supremizers, noting that difference in the basis size does not affect the general form of the problem.

Now, with an expression for each of $\boldsymbol{\eta}, \boldsymbol{u}, \boldsymbol{p}$, and $\boldsymbol{g}$ in terms of their reduced order coefficients, we develop a method for coupling a ROM on Ω_s with a ROM on Ω_f below. The extension to a FEM-ROM coupling would be straightforward and perhaps desired in cases where a high-fidelity expression is needed in parts of the domain; however, we only display the ROM-ROM case here for brevity. We substitute the relationships $\boldsymbol{\eta} = \widetilde{\boldsymbol{\Phi}}_\eta \boldsymbol{\eta_R} + \boldsymbol{\beta}_\eta$, $\boldsymbol{u} = \widetilde{\boldsymbol{\Phi}}_u \boldsymbol{u_R} + \boldsymbol{\beta}_u, \boldsymbol{p} = \widetilde{\boldsymbol{\Phi}}_p \boldsymbol{p_R}, \text{ and } \boldsymbol{g} = \widetilde{\boldsymbol{\Phi}}_g \boldsymbol{g_R}$ into (3.1) and project each equation appropriately. Of course, one could also substitute the reduced order expressions into the continuous equations and then discretize in time, with the same result.

$$\left(\widetilde{\Phi}_u^T M_f + \Delta t \widetilde{\Phi}_u^T K_f\right)\left(\widetilde{\Phi}_u \boldsymbol{u_R}^{n+1} + \boldsymbol{\beta_u}^{n+1}\right) - \Delta t \widetilde{\Phi}_u^T P\left(\widetilde{\Phi}_p \boldsymbol{p_R}^{n+1}\right) -$$
$$\Delta t \widetilde{\Phi}_u^T G_f^T\left(\widetilde{\Phi}_g \boldsymbol{g_R}^{n+1}\right)$$
$$= \Delta t \widetilde{\Phi}_u^T \overline{\boldsymbol{f}}_{\boldsymbol{f}}^{\,n+1} + \widetilde{\Phi}_u^T M_f\left(\widetilde{\Phi}_u \boldsymbol{u_R}^n + \boldsymbol{\beta_u}^n\right),$$
$$\widetilde{\Phi}_p^T P^T\left(\widetilde{\Phi}_u \boldsymbol{u_R}^{n+1} + \boldsymbol{\beta_u}^{n+1}\right) = \mathbf{0},$$
$$\left(\tfrac{1}{\Delta t}\widetilde{\Phi}_\eta^T M_s + \Delta t \widetilde{\Phi}_\eta^T (K_s + L)\right)\left(\widetilde{\Phi}_\eta \boldsymbol{\eta_R}^{n+1} + \boldsymbol{\beta_\eta}^{n+1}\right) + \Delta t \widetilde{\Phi}_\eta^T G_s^T\left(\widetilde{\Phi}_g \boldsymbol{g_R}^{n+1}\right)$$
$$= \Delta t \widetilde{\Phi}_\eta^T \overline{\boldsymbol{f}}_{\boldsymbol{s}}^{\,n+1} + \tfrac{2}{\Delta t}\widetilde{\Phi}_\eta^T M_s\left(\widetilde{\Phi}_\eta \boldsymbol{\eta_R}^n + \boldsymbol{\beta_\eta}^n\right) - \tfrac{1}{\Delta t}\widetilde{\Phi}_\eta^T M_s\left(\widetilde{\Phi}_\eta \boldsymbol{\eta_R}^{n-1} + \boldsymbol{\beta_\eta}^{n-1}\right),$$
$$\tfrac{1}{\Delta t}\widetilde{\Phi}_g^T G_s\left(\widetilde{\Phi}_\eta \boldsymbol{\eta_R}^{n+1} + \boldsymbol{\beta_\eta}^{n+1}\right) - \widetilde{\Phi}_g^T G_f\left(\widetilde{\Phi}_u \boldsymbol{u_R}^{n+1} + \boldsymbol{\beta_u}^{n+1}\right) =$$
$$\tfrac{1}{\Delta t}\widetilde{\Phi}_g^T G_s\left(\widetilde{\Phi}_\eta \boldsymbol{\eta_R}^n + \boldsymbol{\beta_\eta}^n\right).$$

Define reduced order matrices, and then form block matrices as before:

$$\widetilde{M}_s := \widetilde{\Phi}_\eta^T M_s \widetilde{\Phi}_\eta, \quad D_s := K_s + L, \qquad \widetilde{D}_s := \widetilde{\Phi}_\eta^T D_s \widetilde{\Phi}_\eta, \quad \widetilde{G}_s := \widetilde{\Phi}_g^T G_s \widetilde{\Phi}_\eta$$
$$\widetilde{M}_f := \widetilde{\Phi}_u^T M_f \widetilde{\Phi}_u, \quad \widetilde{K}_f := \widetilde{\Phi}_u^T K_f \widetilde{\Phi}_u, \quad \widetilde{G}_f := \widetilde{\Phi}_g^T G_f \widetilde{\Phi}_u, \quad \widetilde{P} := \widetilde{\Phi}_u^T P \widetilde{\Phi}_p$$
$$\boldsymbol{z_R}^{n+1} := \begin{bmatrix} \boldsymbol{p_R}^{n+1} \\ \boldsymbol{g_R}^{n+1} \end{bmatrix}, \quad A_f := \begin{bmatrix} \widetilde{P}^T \\ \widetilde{G}_f \end{bmatrix}, \qquad A_s := \begin{bmatrix} 0_{N_{R,p} \times N_{R,\eta}} \\ \widetilde{G}_s \end{bmatrix}.$$

The system becomes:

$$\left(\widetilde{M}_f + \Delta t \widetilde{K}_f\right)\boldsymbol{u_R}^{n+1} - \Delta t A_f^T \boldsymbol{z_R}^{n+1} = \Delta t \widetilde{\Phi}_u^T \overline{\boldsymbol{f}}_{\boldsymbol{f}}^{\,n+1} + \widetilde{M}_f \boldsymbol{u_R}^n +$$
$$\widetilde{\Phi}_u^T M_f(\boldsymbol{\beta}_u^n - \boldsymbol{\beta}_u^{n+1}) - \Delta t \widetilde{\Phi}_u^T K_f \boldsymbol{\beta}_u^{n+1}$$
$$\left(\tfrac{1}{\Delta t}\widetilde{M}_s + \Delta t \widetilde{D}_s\right)\boldsymbol{\eta_R}^{n+1} + \Delta t A_s^T \boldsymbol{z_R}^{n+1} = \Delta t \widetilde{\Phi}_\eta^T \overline{\boldsymbol{f}}_{\boldsymbol{s}}^{\,n+1} + \tfrac{2}{\Delta t}\widetilde{M}_s \boldsymbol{\eta_R}^n -$$
$$\tfrac{1}{\Delta t}\widetilde{M}_s \boldsymbol{\eta_R}^{n-1} + \tfrac{2}{\Delta t}\widetilde{\Phi}_\eta^T M_s \boldsymbol{\beta}_\eta^n$$
$$- \tfrac{1}{\Delta t}\widetilde{\Phi}_\eta^T M_s \boldsymbol{\beta}_\eta^{n-1} - \left(\tfrac{1}{\Delta t}\widetilde{\Phi}_\eta^T M_s + \Delta t \widetilde{\Phi}_\eta^T D_s\right)\boldsymbol{\beta}_\eta^{n+1}$$
$$\tfrac{1}{\Delta t} A_s \boldsymbol{\eta_R}^{n+1} - A_f \boldsymbol{u_R}^{n+1} =$$
$$\begin{bmatrix} \widetilde{\Phi}_p^T P^T \boldsymbol{\beta_u}^{n+1} \\ \tfrac{1}{\Delta t}\widetilde{G}_s \boldsymbol{\eta_R}^n + \tfrac{1}{\Delta t}\widetilde{\Phi}_g^T G_s \boldsymbol{\beta_\eta}^n - \tfrac{1}{\Delta t}\widetilde{\Phi}_g^T G_s \boldsymbol{\beta_\eta}^{n+1} + \widetilde{\Phi}_g^T G_f \boldsymbol{\beta_u}^{n+1} \end{bmatrix}$$

As in the FEM-FEM coupling, we use the change of variables $\tilde{\boldsymbol{\eta}}_{\boldsymbol{R}}^{\,n+1} := \tfrac{1}{\Delta t}\boldsymbol{\eta_R}^{n+1}$, and $\tilde{\boldsymbol{z}}_{\boldsymbol{R}}^{\,n+1} := \Delta t \boldsymbol{z_R}^{n+1}$. Let $\boldsymbol{w_1}^n, \boldsymbol{w_2}^n, \boldsymbol{w_3}^n$ denote the right hand sides of the above equations, and define the matrices $W_f := \widetilde{M}_f + \Delta t \widetilde{K}_f, W_s := \widetilde{M}_s + \Delta t^2 \widetilde{D}_s$.

With these, the system may be rewritten as:

$$\begin{aligned} W_f \boldsymbol{u_R}^{n+1} - A_f^T \tilde{\boldsymbol{z}}_{\boldsymbol{R}}^{n+1} &= \boldsymbol{w_1}^n, \\ W_s \tilde{\boldsymbol{\eta}}_{\boldsymbol{R}}^{n+1} + A_s^T \tilde{\boldsymbol{z}}_{\boldsymbol{R}}^{n+1} &= \boldsymbol{w_2}^n, \\ A_s \tilde{\boldsymbol{\eta}}_{\boldsymbol{R}}^{n+1} - A_f \boldsymbol{u_R}^{n+1} &= \boldsymbol{w_3}^n. \end{aligned} \tag{5.1}$$

The first two equations of (5.1) may be used to solve for $\boldsymbol{u_R}^{n+1}, \tilde{\boldsymbol{\eta}}_{\boldsymbol{R}}^{n+1}$, and substituting the results into the third equation results in a similar form of the Schur complement system as in the FEM-FEM case:

$$\left(A_f W_f^{-1} A_f^T + A_s W_s^{-1} A_s^T\right) \tilde{\boldsymbol{z}}_{\boldsymbol{R}}^{n+1} = A_s W_s^{-1} \boldsymbol{w_2}^n - A_f W_f^{-1} \boldsymbol{w_1}^n - \boldsymbol{w_3}^n. \tag{5.2}$$

At each time step, then, we solve the Schur complement equation (5.2), and then use the resulting $\tilde{\boldsymbol{z}}_{\boldsymbol{R}}^{n+1}$ to decouple the first two equations of (5.1), solving independently and without iterations between subdomains. We note here that any matrix solves involving the Schur complement matrix may be performed using the conjugate gradient algorithm without having to assemble the Schur matrix directly. However, as all matrices are independent of time, one could also assemble once and perform a factorization at the initial step, using that to solve the system directly at all following time steps.

Our reduced size matrices W_f, W_s are of dimension $N_{R,u} \times N_{R,u}$ and $N_{R,\eta} \times N_{R,\eta}$, and the Schur complement matrix is a square matrix with $N_{R,p} + N_{R,g}$ rows. In the next section, we present numerical results that show the computational speedups gained by solving these smaller systems without sacrificing accuracy.

6. Numerical results

To demonstrate the performance of our coupled formulation, we compare the results of applying our partitioned method to the ROM-ROM system (5.1) and to the FEM-FEM system (3.2) using two numerical tests.

Let $\boldsymbol{\eta_F}, \boldsymbol{u_F}, \boldsymbol{p_F}, \boldsymbol{g_F}$ represent full size FEM coefficient vectors and $\boldsymbol{\eta_R}, \boldsymbol{u_R}, \boldsymbol{p_R}, \boldsymbol{g_R}$ be their reduced order counterparts of size $N_{R,\eta}, N_{R,u}, N_{R,p}$, and $N_{R,g}$ respectively. To simplify notation, we drop the subscript *R* from the sizes, letting N_η, N_u, N_p, N_g refer in this section to the reduced basis sizes examined. When supremizer enrichment is used, the supremizer variables for displacement and velocity are denoted by $\boldsymbol{s_\eta}, \boldsymbol{s_u}$ of size $N_{s,\eta}, N_{s,u}$. For the FEM-FEM solution, the (P_2, P_1) pair is used for velocity and pressure, P_2 for displacement, and P_1 for the LM.

6.1. Analytical solution

We first consider a manufactured solution to the FSI system (2.1)-(2.6), as presented in [4] and solved also in [29]. This simplified problem setting allows more isolated investigation into the performance of each ROM and their coupling without additional complications posed by the physical setting. On $\Omega_f = [0,1] \times [0,1]$ and $\Omega_s = [0,1] \times [1,2]$, define the velocity $\boldsymbol{u} = [u_1, u_2]^T$, pressure p, and displacement $\boldsymbol{\eta} = [\eta_1, \eta_2]^T$ as:

$$
\begin{aligned}
u_1 &= \cos(x+t)\sin(y+t) + \sin(x+t)\cos(y+t) \\
u_2 &= -\cos(x+t)\sin(y+t) - \sin(x+t)\cos(y+t) \\
p &= 2\nu_f(\sin(x+t)\sin(y+t) - \cos(x+t)\cos(y+t)) + 2\nu_s\cos(x+t)\sin(y+t) \\
\eta_1 &= \sin(x+t)\sin(y+t) \\
\eta_2 &= \cos(x+t)\cos(x+t).
\end{aligned}
$$

All parameters are set to 1, and non-homogeneous Dirichlet boundaries are set on each boundary except the side walls of Ω_f, where appropriate Neumann conditions are imposed.

The error in the ROM solution can be traced to two sources: the ability of the snapshots to accurately capture the true solution, and the performance of the ROM in reproducing the behavior of the snapshots. As techniques for obtaining the best snapshots are beyond the scope of this paper, we focus our attention on the second source of error, comparing the ROM solution to the offline FEM solution from which it was derived. The snapshots used are the solutions to the FEM-FEM coupled problem at each time step using the partitioned method presented in Section 3, with $\Delta x = \Delta y = 1/32, \Delta t = 10^{-5}$, and $T_f = 10^{-3}$. This yields a full size system of 8450 DoFs for the velocity and displacement, 1089 DoFs for pressure, and 66 DoFs for the LM. As the number of DoFs for the LM is less than the number of snapshots, we only have 66 singular values shown for the LM in Fig. 1(b), whereas each other variable has 101 singular values as their snapshot matrices contained more rows than columns. The L^2 errors between the FEM solution and the exact solution are on the order of 10^{-7} for velocity and displacement and 10^{-5} for pressure. The H^1 errors for velocity and displacement are on the order of 10^{-4}. We will see that the application of the ROM to each subdomain yields a significant reduction in the number of DoFs while producing similar results.

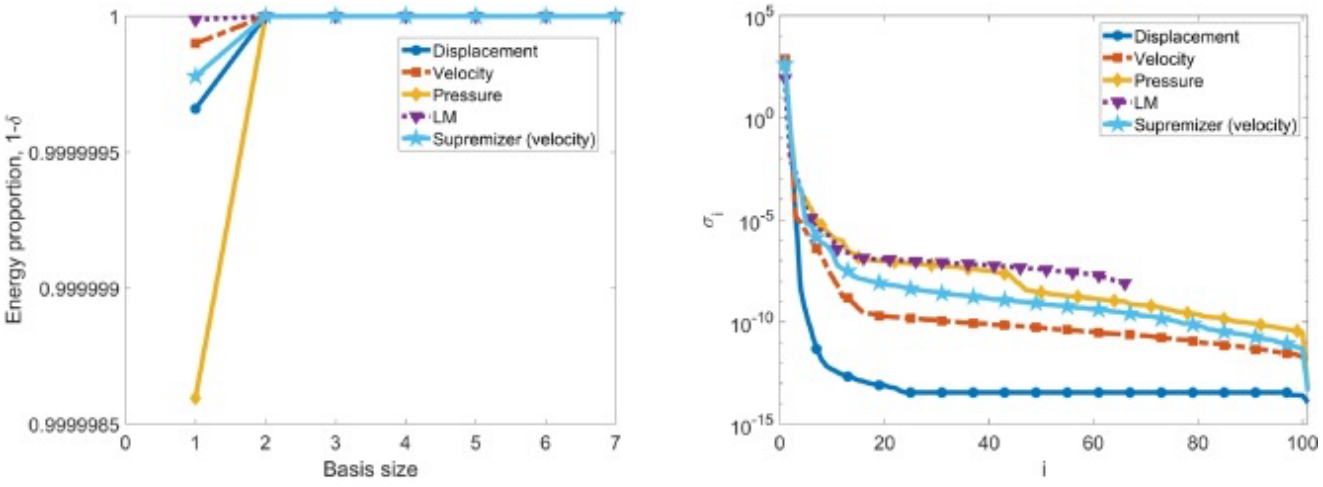

(a) Energy proportion $1-\delta$, (4.1) (b) Singular value decay

Download: Download high-res image (262KB)

Download: Download full-size image

Fig. 1. Energy and singular value decay for the manufactured solution.

To begin our analysis, we observe the behavior of the singular values of each variable's snapshots. For POD to be applied, the singular values of the snapshots must decay quickly enough so that most of the energy is captured in a small subset of the modes. In Fig. 1, we see that the singular values do decrease sharply, and over 99.999% of the snapshot energy is contained in just the first mode for each variable (Fig. 1(a)). Singular values of the displacement supremizers are not shown as they experience the same rapid decay as the other variables, and they will later be shown to be superfluous in the formulation. As the singular values of the pressure and LM decay similarly (Fig. 1(b)), we simplify the number of basis sizes to consider varying by setting $N_p = N_g$ in all of the following calculations.

In analyzing the performance of our scheme, we examine the error between a ROM-ROM or FEM-ROM solution and the FEM-FEM solution for each variable. We denote by $\widehat{\boldsymbol{u}}_{\boldsymbol{R}}$ the projection of the ROM velocity coefficients back into the FEM space; i.e., $\widehat{\boldsymbol{u}}_{\boldsymbol{R}} := \widetilde{\boldsymbol{\Phi}}_u \boldsymbol{u}_{\boldsymbol{R}} + \boldsymbol{\beta}_{\boldsymbol{u}}$ for ROM coefficients $\boldsymbol{u}_{\boldsymbol{R}}$. We then measure errors between $\widehat{\boldsymbol{u}}_{\boldsymbol{R}}$ and $\boldsymbol{u}_{\boldsymbol{F}}$ at a given time t, where $\boldsymbol{u}_{\boldsymbol{F}}$ is the reference solution computed by the FEM-FEM coupling. Projections $\widehat{\boldsymbol{\eta}}_{\boldsymbol{R}}$ and $\widehat{\boldsymbol{p}}_{\boldsymbol{R}}$ are similarly defined so that the L^2 errors at time t are:

$$||\widehat{\boldsymbol{\eta}}_{\boldsymbol{R}}(t) - \boldsymbol{\eta}_{\boldsymbol{F}}(t)||_{0,\Omega_s}, \quad ||\widehat{\boldsymbol{u}}_{\boldsymbol{R}}(t) - \boldsymbol{u}_{\boldsymbol{F}}(t)||_{0,\Omega_f}, \quad ||\widehat{\boldsymbol{p}}_{\boldsymbol{R}}(t) - \boldsymbol{p}_{\boldsymbol{F}}(t)||_{0,\Omega_f}.$$

In the plots, we leave off the notation of the subdomain Ω_s, Ω_f on the norms as the appropriate

subdomain will be clear from context. To examine the effect of supremizer enrichment on the accuracy and stability of the ROM-ROM formulation, we turn to Fig. 2 and examine the L^2 errors versus time over the interval $t \in [10^{-5}, 10^{-3}]$.

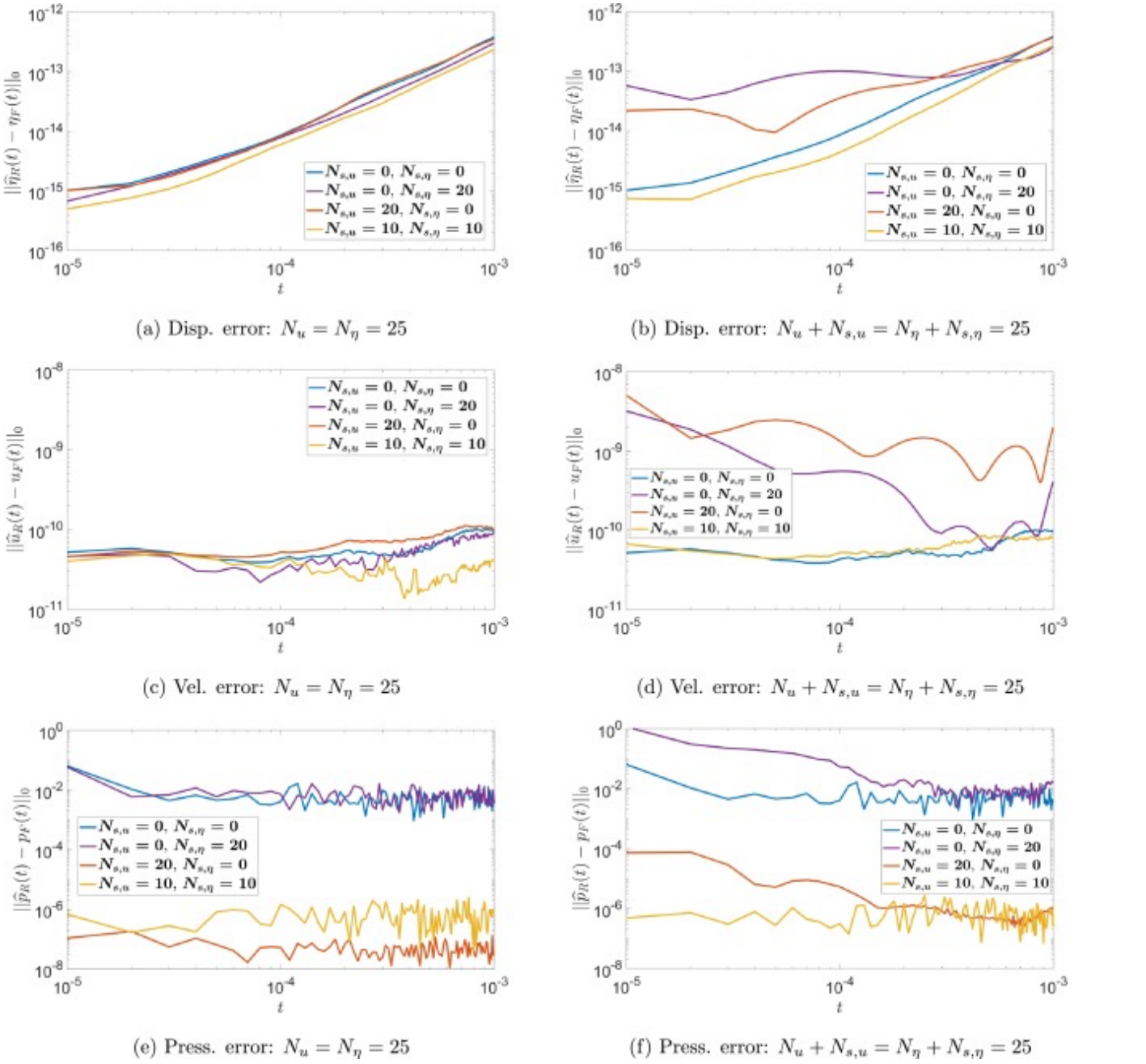

(a) Disp. error: $N_u = N_\eta = 25$

(b) Disp. error: $N_u + N_{s,u} = N_\eta + N_{s,\eta} = 25$

(c) Vel. error: $N_u = N_\eta = 25$

(d) Vel. error: $N_u + N_{s,u} = N_\eta + N_{s,\eta} = 25$

(e) Press. error: $N_u = N_\eta = 25$

(f) Press. error: $N_u + N_{s,u} = N_\eta + N_{s,\eta} = 25$

Download: Download high-res image (739KB)

Download: Download full-size image

Fig. 2. L^2 errors over time for the manufactured solution. Pressure and LM reduced basis sizes are fixed at $N_p = N_g = 10$. Subfigures (a), (c), (e) show supremizers used in addition to the POD basis

functions, while subfigures (b), (d), (f) show supremizers substituted in place of POD basis functions. (For interpretation of the colors in the figure(s), the reader is referred to the web version of this article.)

For each subplot, we fix $N_p = N_g = 10$. In the left column, each formulation sets $N_u = N_\eta = 25$ and examines the effect of adding supremizer basis functions to the POD basis for either velocity, displacement, or both. The total number of supremizers is chosen to be $N_p + N_g = 20$ to match the number of total constraints. In the right column, we fix the size of the enriched velocity and displacement spaces, $N_u + N_{s,u}$ and $N_\eta + N_{s,\eta}$ at 25. Thus, any supremizers that are utilized are substituted for POD basis functions.

Overall, formulations in which supremizers are added to the POD basis (Figs. 2(a), 2(c), 2(e)) instead of substituted for POD basis functions (Figs. 2(b), 2(d), 2(f)) perform better, as would be expected since the overall basis size is increased. Supremizers influence most the accuracy of the pressure; Fig. 2(e) shows that adding supremizers to only the displacement space does not change the behavior of the pressure; adding supremizers to both spaces improves the errors by several orders of magnitude, and adding supremizers to only the velocity improves still more. As the displacement has no direct interaction with the pressure, it needs no extra stabilization with respect to the pressure space getting too large. In general, it seems some supremizers must be utilized in the velocity space for the pressure errors to be reasonable, and the more supremizers that are used in the velocity space, the better the pressure behaves. However, we may also observe that adding supremizers does not greatly affect the behavior of the velocity or displacement (Figs. 2(a)-2(d)). The increases in error by orders of magnitude displayed in Figs. 2(b) and 2(d) may be traced to the fact that the dimension of the POD basis (N_u or N_η) in these scenarios is only 5, due to the fact that 20 supremizer basis functions were substituted for POD basis functions. For this problem, the POD basis needs to retain a minimum of roughly 15 modes to see the optimal error size for velocity and displacement, as can be seen by the yellow line representing $N_{s,u} = N_{s,\eta} = 10$ in the same subfigures.

Additionally, we observe that all ROM formulations show stability over time. The one exception at first glance looks to be the displacement (Figs. 2(a) and 2(b)), but as the initial errors are close to machine precision, this may be due to the accumulation of time integration errors from using Backward Euler to update the subsystems rather than instability inherent in the coupled formulation.

Based on Fig. 2, we choose to focus on enriching only the reduced velocity space by adding

supremizers into the POD basis. We continue to examine the effect of supremizers on the error in Fig. 3. The following plots now consider the error between the ROM and FEM solutions at the final time $T_f = 10^{-3}$. In each subplot, we fix the total size of the enriched, reduced velocity subspace $(N_u + N_{s,u})$ at 100. Each subplot demonstrates a different combination of N_η and $N_p = N_g$, and we observe the effect on the pressure and velocity errors of varying the proportion of POD velocity basis functions to supremizer basis functions. As the displacement error is much more stable with respect to the basis sizes, we look to the pressure and velocity errors as representative of the behavior of the problem as a whole. Consistently among each of the three subfigures, formulations that weigh heavily in favor of POD basis functions, utilizing few to no supremizer functions, perform poorly in terms of pressure error. As the number of supremizers increases, the pressure error tends to improve. The only exception to this is the case with $N_u = 5, N_{s,u} = 95$; as we have previously observed, the POD velocity basis needs to retain at least 15 modes for best performance. Velocity error is less affected by the use of supremizers; as long as more than 5 POD basis functions are retained, all of the velocity errors are on the order of 10^{-10}, with even the "worst case" scenario of $N_u = 5$ resulting in a velocity error only one order of magnitude greater than the rest. Overall, we observe from these figures that a mixed balance between velocity and supremizer functions seems to achieve the optimal errors for this scenario. Fig. 3(c) displays the "best" results, in the sense that errors of similar sizes can be obtained while using smaller basis sizes for the displacement, pressure and LM.

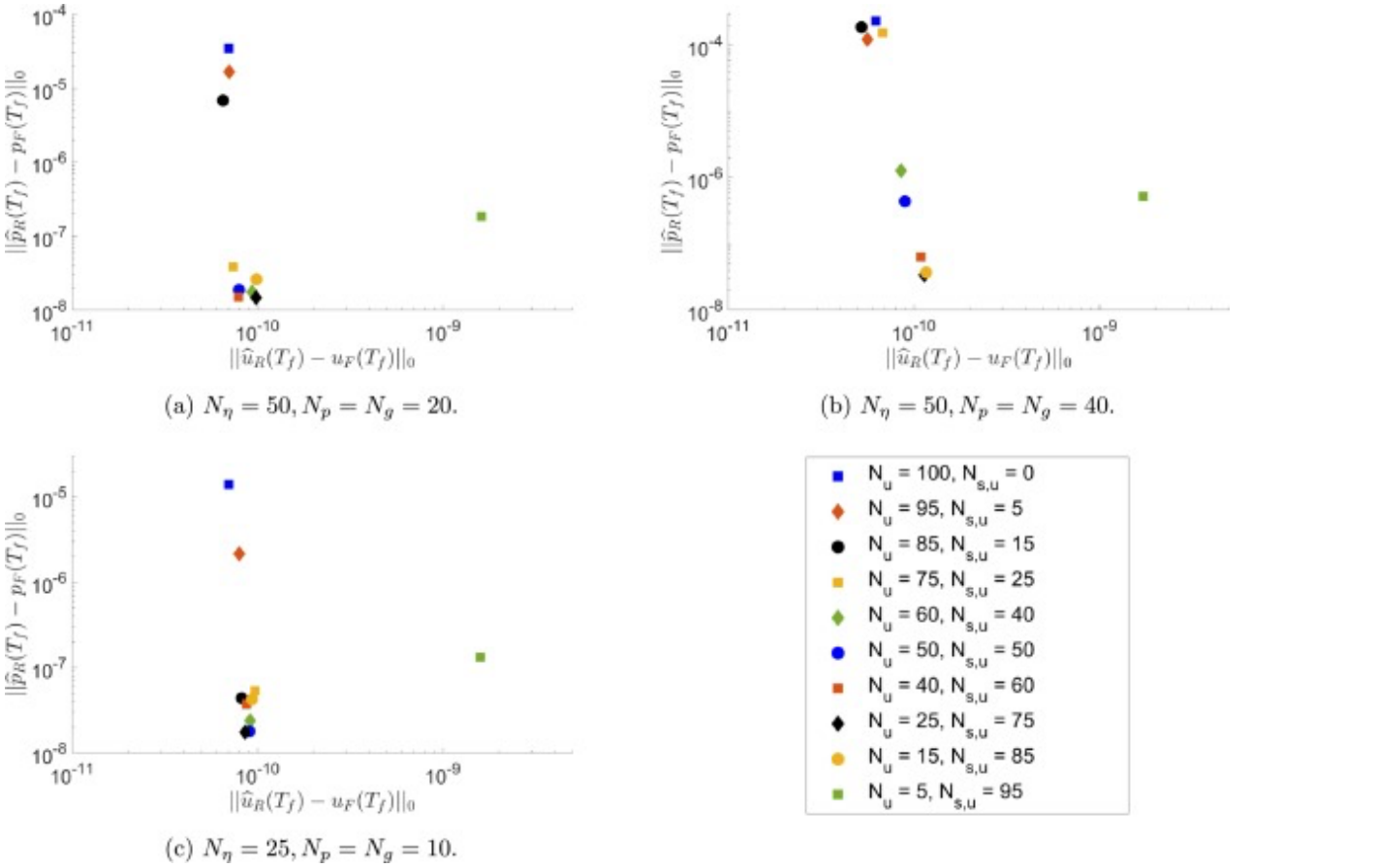

Download: Download high-res image (239KB)

Download: Download full-size image

Fig. 3. Pressure and velocity L^2 errors for the manufactured solution for $N_u + N_{s,u} = 100$.

Fig. 4 examines the behavior of the velocity and pressure errors with respect to the size of the POD velocity basis N_u. Displacement errors behave similarly to velocity errors, and are therefore not displayed. Without supremizers, the errors experience large spikes at smaller values of N_u, as seen in Figs. 4(a)-4(b). The only cases which do not experience the large spikes are those in which $N_p = N_g \leq 10$. In the next row, supremizers are added to the velocity basis with $N_{s,u} = N_p$. For both "small" (4(c)) and "medium" (4(d)) values of N_p, the spikes in the error disappear. Again, although only pressure is plotted, the same improvement in errors is experienced by the velocity and the displacement as well. Lastly, as the pressure and LM are grouped in our formulation, we consider using $N_{s,u} = N_p + N_g$ in Figs. 4(e)-4(f). Without supremizers, the smallest pressure error was $O(10^{-5})$; adding supremizers gives values on the order of 10^{-7} or 10^{-8}. The best case scenario is when $N_{s,u} = N_p + N_g$, and the seemingingly oscillatory nature of the errors is all within the same order of magnitude (compare the y-scale on

Figs. 4(b), 4(d), and 4(f)).

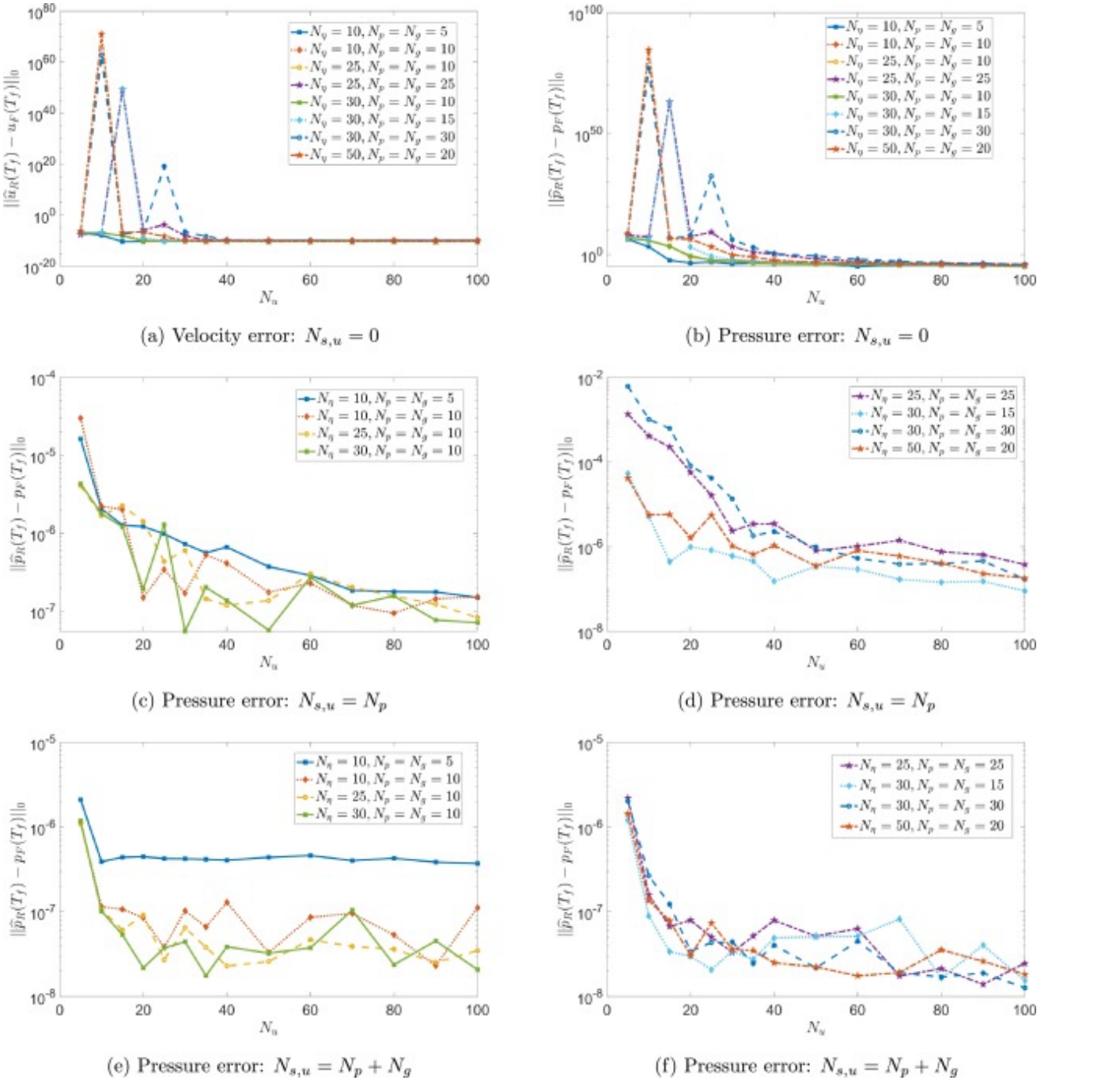

(a) Velocity error: $N_{s,u} = 0$

(b) Pressure error: $N_{s,u} = 0$

(c) Pressure error: $N_{s,u} = N_p$

(d) Pressure error: $N_{s,u} = N_p$

(e) Pressure error: $N_{s,u} = N_p + N_g$

(f) Pressure error: $N_{s,u} = N_p + N_g$

Download: Download high-res image (798KB)

Download: Download full-size image

Fig. 4. L^2 errors vs velocity POD basis size for the manufactured solution. Velocity and pressure errors without supremizers are in subplots (a) and (b). Pressure errors with supremizers are in subplots (c)-(f). Smaller basis sizes N_p for formulations with supremizers are shown in subplots

(c) and (e); larger N_p in (d) and (f). No supremizers are utilized in the displacement space; i.e., $N_{s,\eta} = 0$.

Lastly, since the formulation hinges on solving the reduced order Schur complement equation, we want to observe the conditioning of this system. See [16] for a discussion on and bounds for the condition number of the Schur complement matrix in the FEM case. Fig. 5 shows the condition number of the Schur complement matrix in 5(a) and the preconditioned Schur complement matrix in 5(b) with respect to N_u, for the case $N_{s,u} = N_p + N_g$. Without preconditioning, the worst condition numbers are on the order of 10^4, and using the fluid half of the Schur complement matrix as a preconditioner reduces the condition number even more. In either scenarios, we observe numerically that the system is not ill-conditioned in practice.

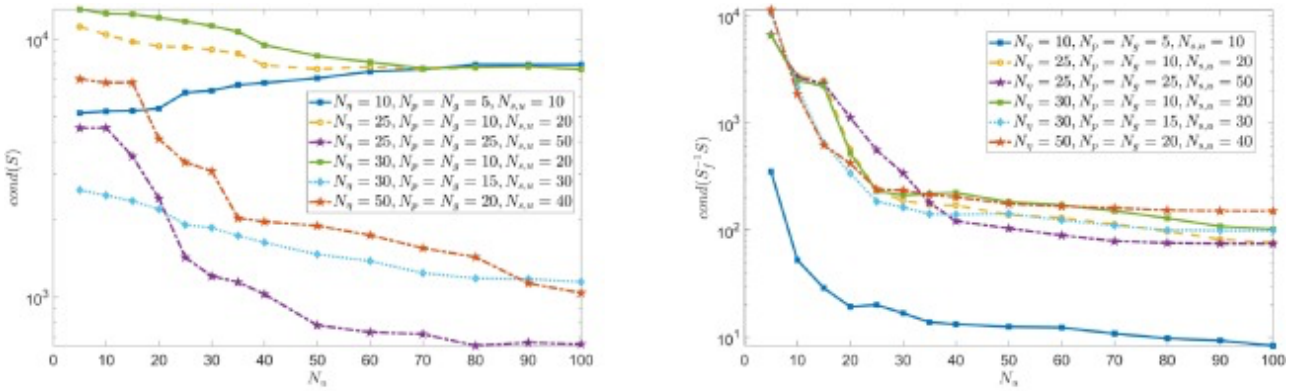

(a) cond(S) (b) cond(S) preconditioned

Download: Download high-res image (308KB)

Download: Download full-size image

Fig. 5. Condition numbers of Schur complement matrix (a) and pre-conditioned Schur complement matrix (b) for the manufactured solution, for $N_{s,u} = N_p + N_g$.

6.2. Blood flow example

The second numerical test considered is a pressure wave propagation which demonstrates the added mass effect (see [10]). We consider both a ROM-ROM and a FEM-ROM coupling for this problem, dedicating most discussion to the ROM-ROM coupling. The domain considered is $\Omega_f = [0, 6] \times [0, 0.5]$ and $\Omega_s = [0, 6] \times [0.5, 0.6]$, with parameters $\rho_f = 1, \nu_f = 0.035, \rho_s = 1.1, \nu_s = 1.15 \times 10^6, \lambda = 1.7 \times 10^6$. These parameters are representative of a blood flow problem, and all units are given in the centimeter-gram-second

(CGS) system. On Ω_s, we enforce homogeneous Dirichlet conditions at $x = 0$ and $x = 6$, and zero traction forces on the upper boundary $y = 0.6$. For the fluid domain we impose zero traction force on the right boundary $x = 6$, homogeneous Dirichlet on $y = 0$, and on the left boundary we implement a Neumann condition given by a sinusoidal pressure that reaches a maximal amplitude of 2×10^4 over 5×10^{-3} seconds, namely $P(t) = 2 \times 10^4 \sin\left(\frac{\pi t}{5 \times 10^{-3}}\right)$. The mesh size is $\Delta x = \Delta y = 0.025$ with $\Delta t = 1.25 \times 10^{-4}$ and $T_f = 0.015$. This domain yields $39442, 8658, 5061$, and 482 DoFs for velocity, displacement, pressure, and LM respectively. Additionally, a zeroth-order term $c_0 \eta$ is added to the structural equation (2.3) for $c_0 = 4 \times 10^6$.

6.2.1. ROM-ROM coupling

The maximum reduced basis size for each variable is 120 since the snapshot matrices contain 120 columns, corresponding to the total number of time steps. As in the manufactured solution, we reduce the LM to the same size as the pressure, i.e., $N_p = N_g$. Using a full size LM space produces unreasonably large errors. Likely, this is because the size of the joint pressure/LM is too large in comparison with the displacement/velocity, causing a discrete inf-sup violation.

In Fig. 6, we check that the snapshot matrix has singular values decaying quickly enough to justify the use of POD. Fig. 6(b) shows that each of the four variables does experience the requisite decay; after roughly 50 modes, the singular values are static. Viewed from the perspective of energy retained by the basis size, we see in Fig. 6(a) that all variables retain roughly 90% of the energy by 3 modes, and approximately 100% by 6 modes. Thus, we conclude that implementing POD ROMs for these variables is valid.

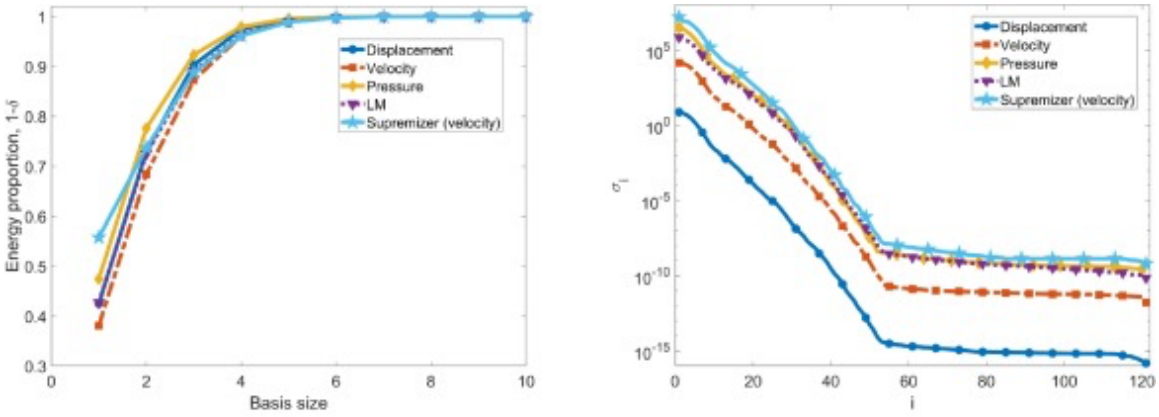

(a) Energy proportion, $1 - \delta$ (4.1) (b) Singular value decay

Download: Download high-res image (235KB)

Download: Download full-size image

Fig. 6. Energy and singular value decay for the blood flow problem.

In Fig. 7, Fig. 8, we compare profiles of the pressure and the vertical solid deformation at times t=0.005, 0.010, and 0.015. In the top rows are profiles obtained using the FEM-FEM coupling, contrasted with the ROM-ROM coupling in the second rows with $N_\eta = 50, N_u = 90, N_p = N_g = 40$. No supremizers are used here as the POD basis sizes used are large. The third rows show the difference between the ROM-ROM and FEM-FEM solutions, with the pressure on the order of 10^{-4} or 10^{-5} and the displacement on the order of 10^{-12} or 10^{-13}. The FEM-FEM results may be compared to similar results in papers such as [10].

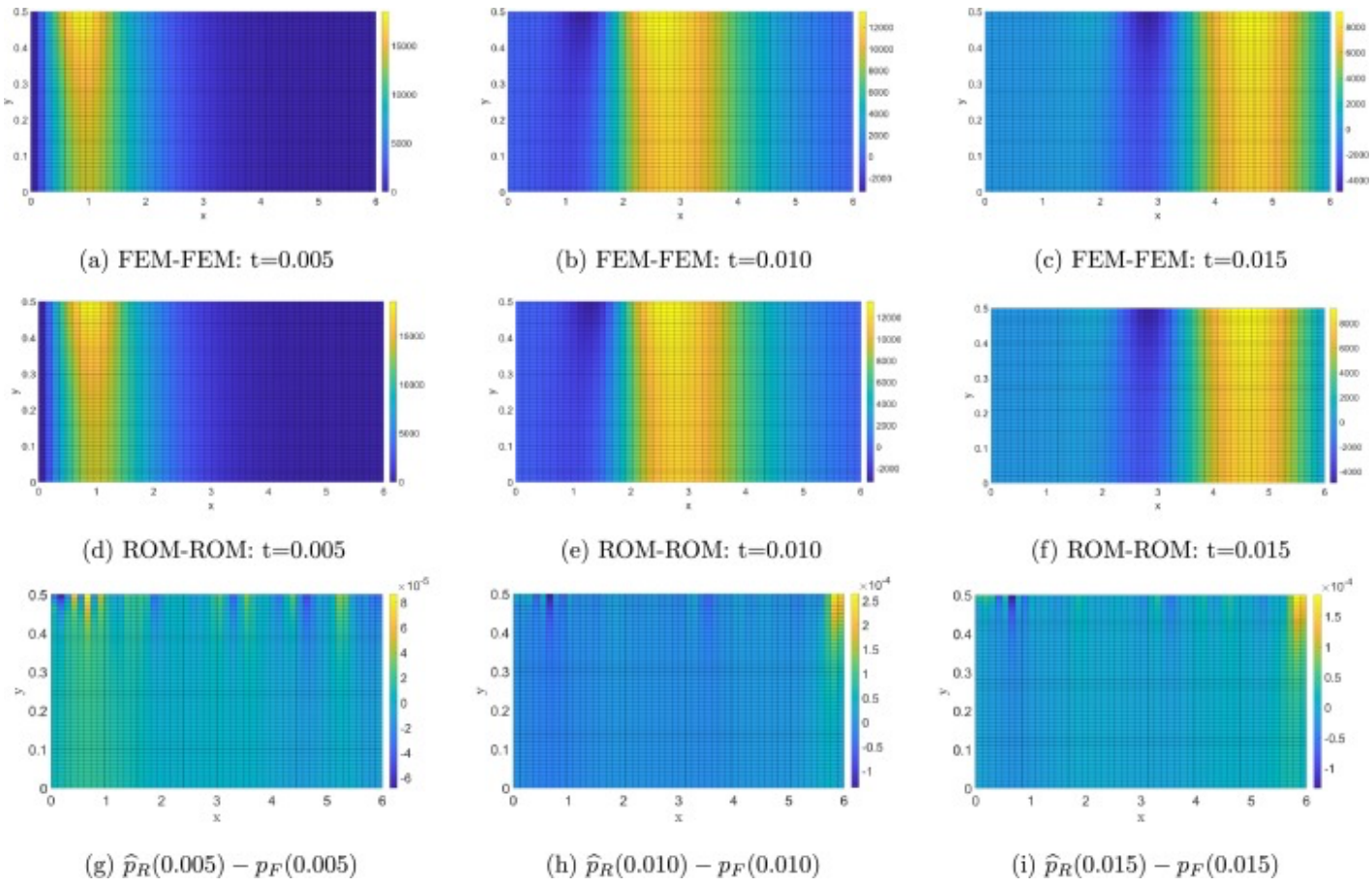

Download: Download high-res image (1MB)

Download: Download full-size image

Fig. 7. Pressure profiles at t=0.005, t=0.01, and t=0.015 for FEM-FEM and ROM-ROM couplings for the blood flow problem. ROM-ROM results shown for $N_u = 90, N_p = N_g = 40, N_\eta = 50$. Subfigures (g)-(i) show the difference between the ROM and FEM solutions, with the y-axis on the scale of 10^{-4} or 10^{-5}.

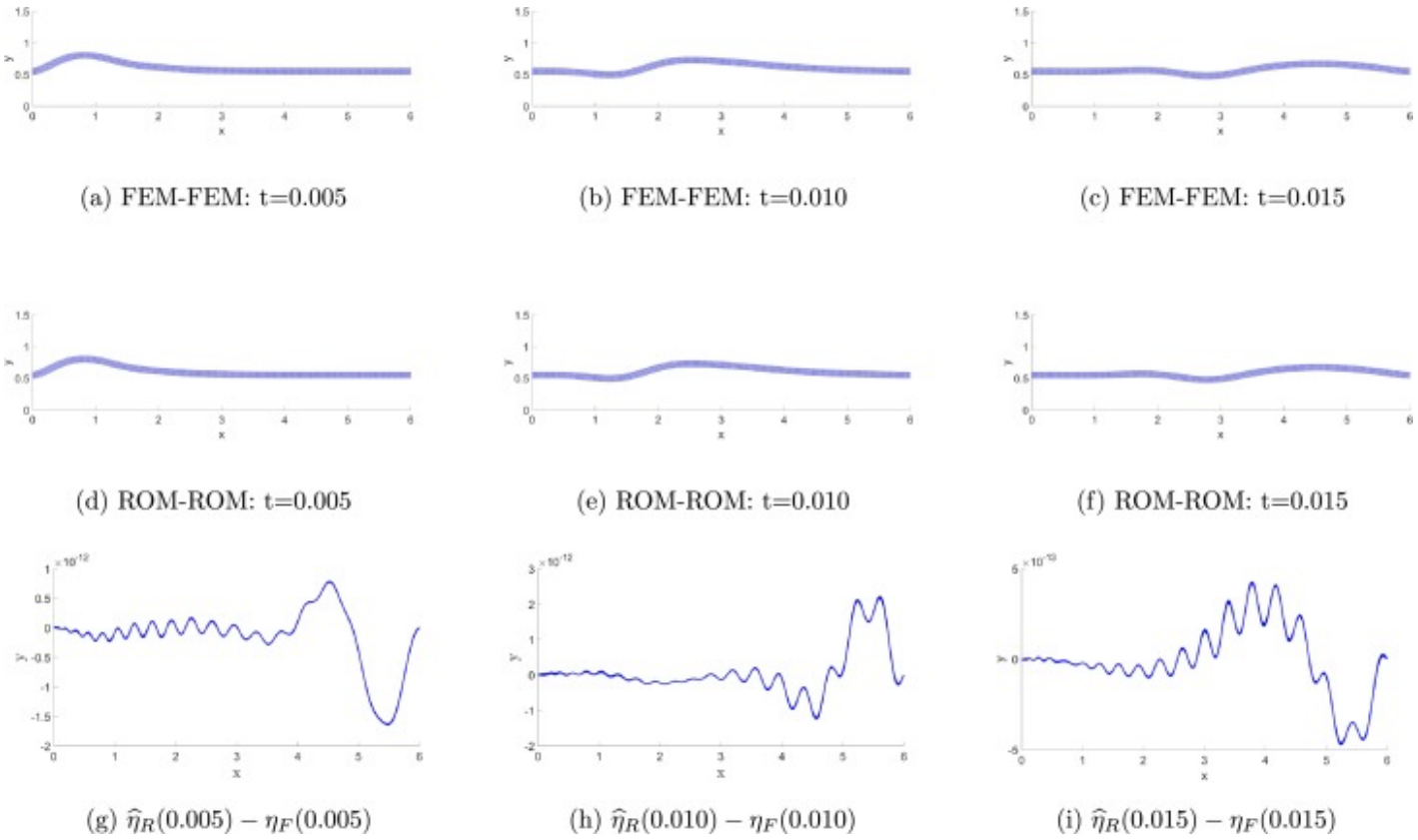

(a) FEM-FEM: t=0.005 (b) FEM-FEM: t=0.010 (c) FEM-FEM: t=0.015

(d) ROM-ROM: t=0.005 (e) ROM-ROM: t=0.010 (f) ROM-ROM: t=0.015

(g) $\widehat{\eta}_R(0.005) - \eta_F(0.005)$ (h) $\widehat{\eta}_R(0.010) - \eta_F(0.010)$ (i) $\widehat{\eta}_R(0.015) - \eta_F(0.015)$

Download: Download high-res image (351KB)

Download: Download full-size image

Fig. 8. Profiles of the solid deformation at t=0.005, t=0.010, and t=0.015 for FEM-FEM and ROM-ROM couplings for the blood flow problem. ROM-ROM results shown for $N_u = 90, N_p = N_g = 40, N_\eta = 50$. All displacements are magnified by a factor of 5. Subfigures (g)-(i) represent the difference between the ROM and FEM solutions, with the y-axis on the scale of 10^{-12} or 10^{-13}.

Next, we quantify the errors by observing the behavior of the L^2 errors with respect to the velocity POD basis size N_u. As in the manufactured solution, displacement errors behave similarly to the velocity errors but are less affected by changes in basis size, so we omit those plots here. The first row of Fig. 9 shows velocity and pressure errors without supremizers (9(a)-9(b)). The error spikes observed without supremizers are remedied by adding $N_{s,u} = N_p$ supremizers to the velocity space, as observed in Figs. 9(c)-9(d). Clearly, supremizers are needed to address both the velocity and pressure errors, although we note that formulations with a "small" pressure basis size ($N_p \approx 10$) did not experience the spikes originally. Figs. 9(d)-9(f)

show that any case utilizing supremizers performs rather similarly with regards to the pressure error and remedies the spikes seen without supremizers. Using $N_{s,u} = N_p$ (9(d) and 9(f)), no meaningful gains are observed by the addition of supremizers to the displacement space. Again, the best behavior is observed when $N_{s,u} = N_p + N_g$ in (9(e)), and the size of the displacement space N_η still does not meaningfully affect results. Unlike the manufactured solution, we observe that the larger pressure reduced basis sizes $(N_p = N_g = 50)$ produce the best results for both velocity and for pressure. For example, with $N_p = N_g = 50$, roughly $N_u \approx 50$ is required to reach the best errors for that formulation, whereas for $N_p = N_g = 25$, only approximately 30 POD basis functions are needed for reaching the lowest error attainable by that formulation. In general, we see a trade-off: increasing N_p will result in a smaller error, but it requires a larger N_u to reach that optimal error.

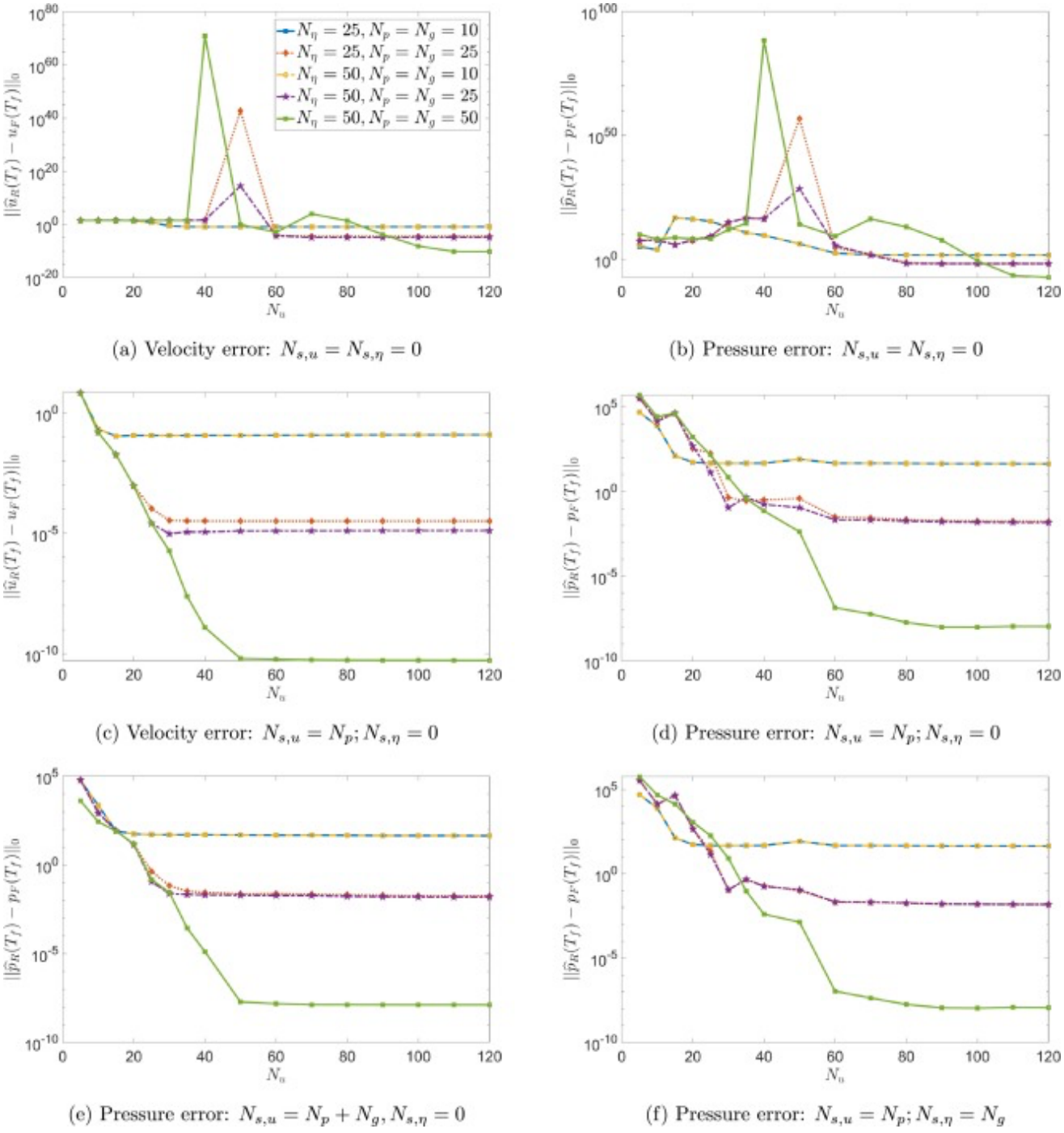

(a) Velocity error: $N_{s,u} = N_{s,\eta} = 0$

(b) Pressure error: $N_{s,u} = N_{s,\eta} = 0$

(c) Velocity error: $N_{s,u} = N_p; N_{s,\eta} = 0$

(d) Pressure error: $N_{s,u} = N_p; N_{s,\eta} = 0$

(e) Pressure error: $N_{s,u} = N_p + N_g, N_{s,\eta} = 0$

(f) Pressure error: $N_{s,u} = N_p; N_{s,\eta} = N_g$

Download: Download high-res image (626KB)

Download: Download full-size image

Fig. 9. L^2 errors for velocity and pressure with respect to N_u for the blood flow problem. The legend in subfigure (a) applies to each subfigure. Subfigures (a) and (b) display results without any supremizers; while subfigures (c)-(f) include different combinations of supremizers.

To further examine the effect of the supremizers, Fig. 10 displays pressure and velocity errors for various combinations of N_u and $N_{s,u}$, such that $N_u + N_{s,u} = 100$. We fix $N_\eta = 50, N_p = N_g = 50$, and $N_{s,\eta} = 0$. Again, we focus on only utilizing supremizers in the velocity space. From the plot, we observe that weighting the formulation heavily in favor of supremizers affects both velocity and pressure error negatively; the best errors are achieved with a combination of POD and supremizer functions in the reduced velocity space. This agrees with our findings in the manufactured solution; using a combination of POD and supremizer functions is likely the best choice, but the proper balance between them is problem dependent. Another point of interest in this plot is the sensitivity of the velocity in this problem; for the manufactured solution in Fig. 3 the velocity errors are all within an order of magnitude. In this blood flow example, using $N_u \leq 25$ produces much larger errors for the velocity, showing that it takes more POD modes in this problem to capture the main behavior of the velocity than the manufactured solution required.

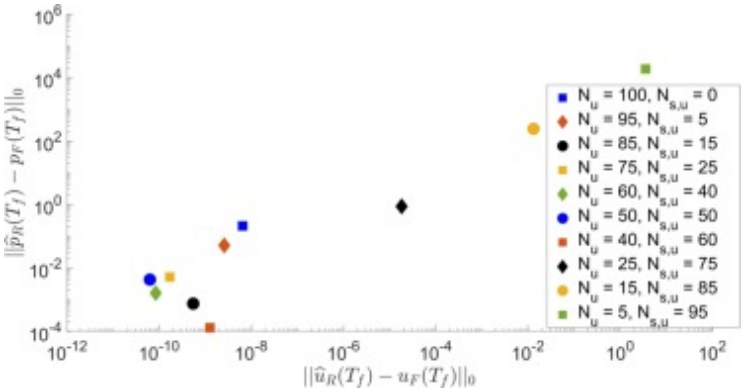

Download: Download high-res image (57KB)

Download: Download full-size image

Fig. 10. Pressure versus velocity errors for the blood flow problem, shown for combinations of $N_u + N_{s,u} = 100$. $N_\eta = N_p = N_g = 50$; $N_{s,\eta} = 0$.

Fig. 11 displays Pareto plots, where each subplot shows the L^2 error versus runtime for displacement (11(a)), velocity (11(b)), and pressure (11(c)). We show the best scenarios from Fig. 9, namely, the case where $N_{s,u} = N_p + N_g$ and $N_{s,\eta} = 0$, and each point on the scatterplot represents a different value of N_u. For this particular problem, the right hand side is precisely zero, and so we are able to save time by not constructing the right hand side at each time step, giving lower average run times. With the FEM time around 40.7 seconds, we see that the ROM solutions are computed in anywhere from 1.7 to 6 seconds, which is about 4.2% to 14.7% of the

time of the FEM formulation. As observed in Fig. 9, the formulation with $N_p = N_g = 50$ yields the best results in terms of error. These Pareto plots support the use of ROMs: the ROM-ROM system produces similar results to the FEM-FEM solution while significantly reducing the size of the algebraic system and the computational time required.

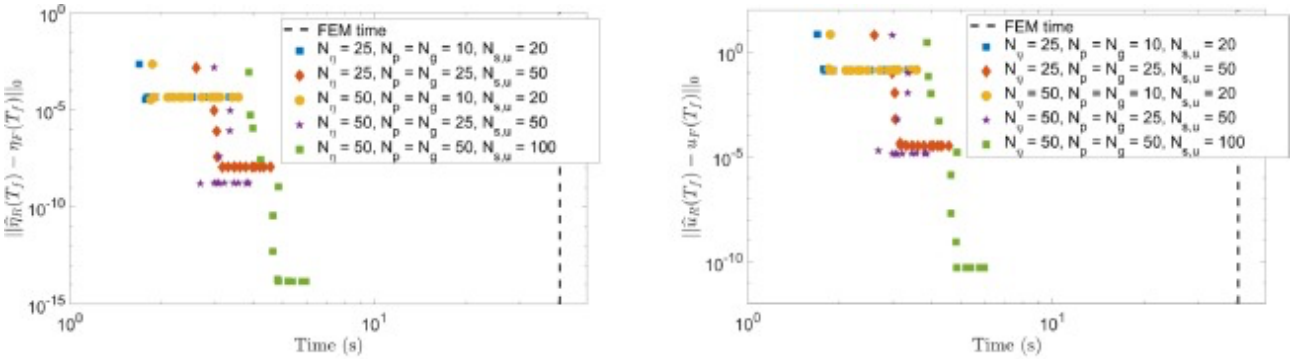

(a) Displacement error, varying N_u

(b) Velocity error, varying N_u

(c) Pressure error, varying N_u

Download: Download high-res image (325KB)

Download: Download full-size image

Fig. 11. L^2 errors versus runtime for the blood flow problem. Each point represents a different choice of N_u. Each variation is able to produce several reasonable/optimal errors in roughly 4-15% of the original FEM time, 40.7 seconds.

Lastly, in Fig. 12 we again observe that the condition number of the Schur complement matrix falls within a reasonable range. More work needs to be done to develop a better preconditioner in this scenario, but even without the preconditioner the most ill-conditioned formulation observed for reasonable basis sizes is on the order of 10^5.

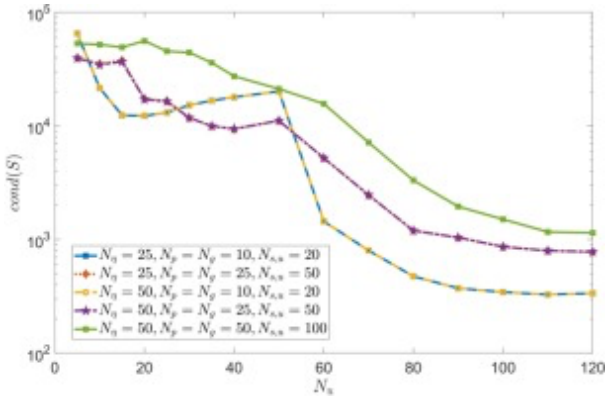

Download: Download high-res image (56KB)

Download: Download full-size image

Fig. 12. Condition numbers of Schur complement matrix for the blood flow problem, with $N_{s,u} = N_p + N_g$.

6.2.2. FEM-ROM coupling

We briefly consider the performance of a coupled FEM-ROM model, using the full order model on Ω_s and the reduced order model on Ω_f. As in the ROM-ROM coupling, we reduce the LM space and set $N_g = N_p$, $N_{s,u} = N_p + N_g$, and $N_{s,\eta} = 0$. The errors versus N_u are shown for each variable in Fig. 13, and errors versus runtime are shown in Fig. 14. We employ the notation $\eta_{F,R}$ to refer to the displacement calculated by the FEM-ROM model, which is already in the full sized FEM space, and calculate its error against the displacement η_F computed by the FEM-FEM model. Comparing the FEM-ROM errors in Fig. 13 with those produced by the ROM-ROM model for a similar configuration in Fig. 9, we see that the use of a ROM or a FEM on Ω_s produces very similar results. Comparing the runtimes in Fig. 11, Fig. 14, both couplings provide computational savings over the FEM-FEM model and achieve the same level of errors; however, the ROM-ROM coupling is able to achieve these results in roughly 2-7 seconds while the FEM-ROM coupling takes about 13-20 seconds. For this model, using a ROM on both subdomains with a large enough N_p appears to be the optimal choice in terms of producing high quality approximations with the shortest computational time.

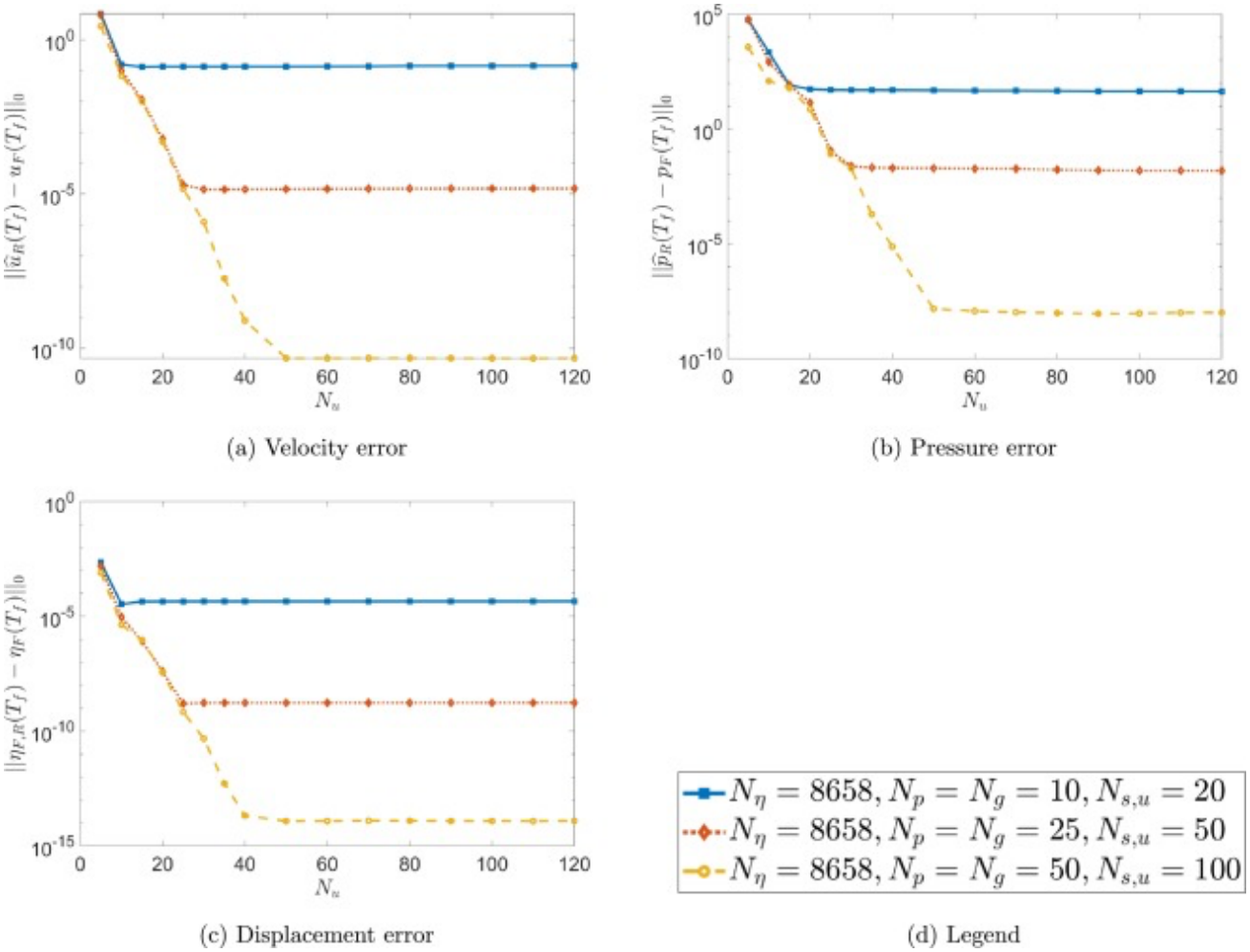

(a) Velocity error (b) Pressure error

(c) Displacement error (d) Legend

Download: Download high-res image (336KB)

Download: Download full-size image

Fig. 13. L^2 errors with respect to N_u for the blood flow problem, with a FEM on Ω_s and ROM on Ω_f. The notation $\eta_{F,R}$ in subplot (c) refers to the displacement calculated by the FEM-ROM model, which is already in the full sized FEM space.

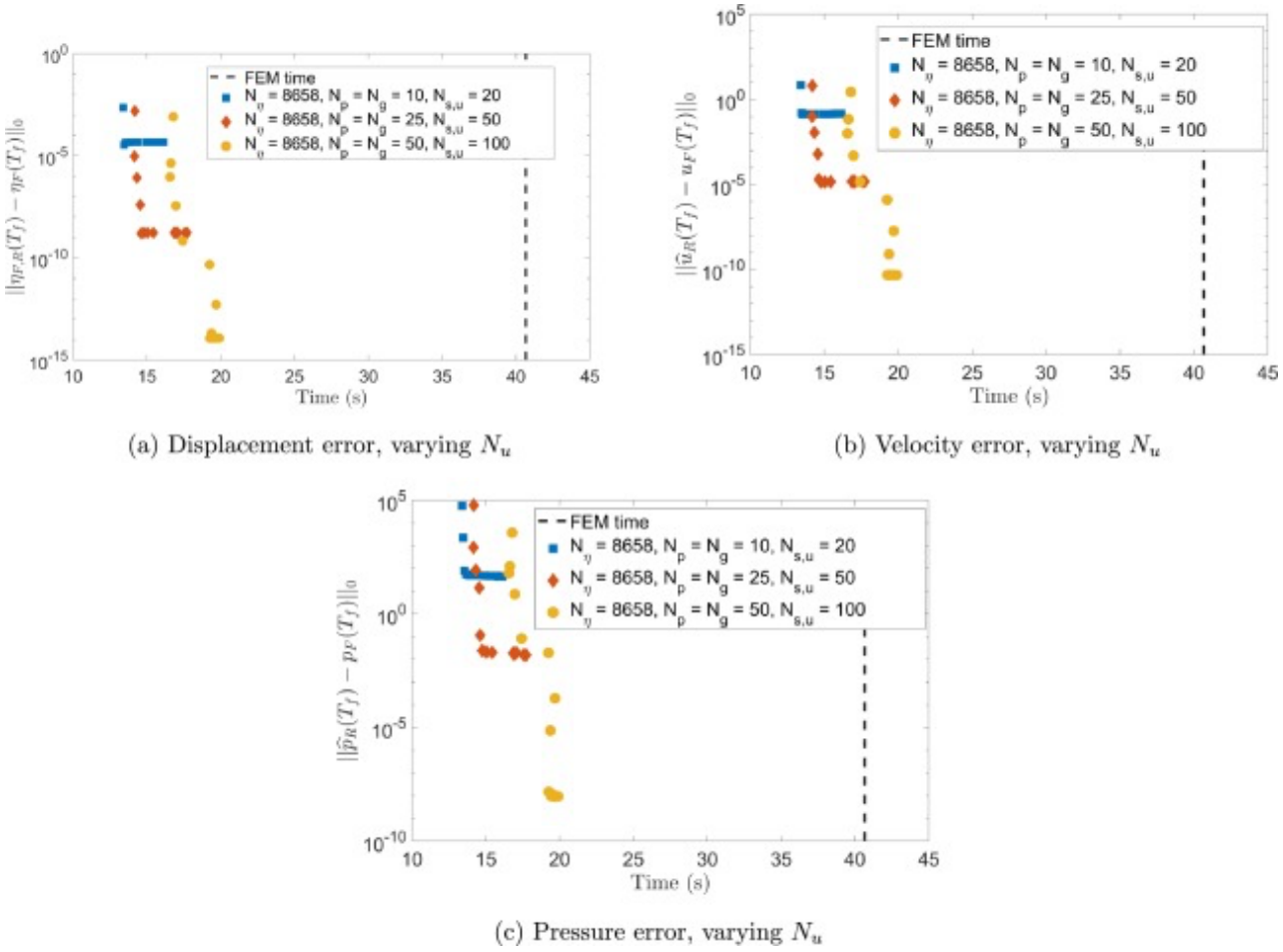

(a) Displacement error, varying N_u

(b) Velocity error, varying N_u

(c) Pressure error, varying N_u

Download: Download high-res image (325KB)

Download: Download full-size image

Fig. 14. L^2 errors versus runtime for the blood flow problem, with a FEM on Ω_s and ROM on Ω_f. Each point represents a different choice of N_u. Each variation is able to produce several reasonable/optimal errors in roughly 32-48% of the original FEM time, 40.7 seconds.

6.3. Parametric ROM-ROM coupling

Lastly, we examine the performance of a ROM-ROM coupling on a parametric problem. Using the blood flow example described in Section 6.2, we set $\Delta t = 1.25 \times 10^{-4}$ and $T_f = 0.01$ and treat the densities as the variable parameters. Letting $\rho_f, \rho_s \in (0, 3]$, we create four sets of snapshots, computed at the values $(\rho_f, \rho_s) = (0.3, 1.1), (1.5, 2.8), (1.9, 0.7)$, and $(2.4, 2.6)$. This yields a total of 324 snapshots, on which we perform SVD to create the ROM bases. For the ROM-ROM coupling, we use the test parameter value $(\rho_f, \rho_s) = (1, 1.1)$.

We observe in Fig. 15 that the size of the displacement space has more effect here than in the non-parametric ROMs. As expected, larger spaces produce better errors, and although the errors are not as low as in the non-parametric ROMs, we still observe a decrease in errors and stabilization from the supremizers added into the velocity space. Likely, these estimates would be improved by enriching the snapshots to better sample the parameter space, which could be examined in future work.

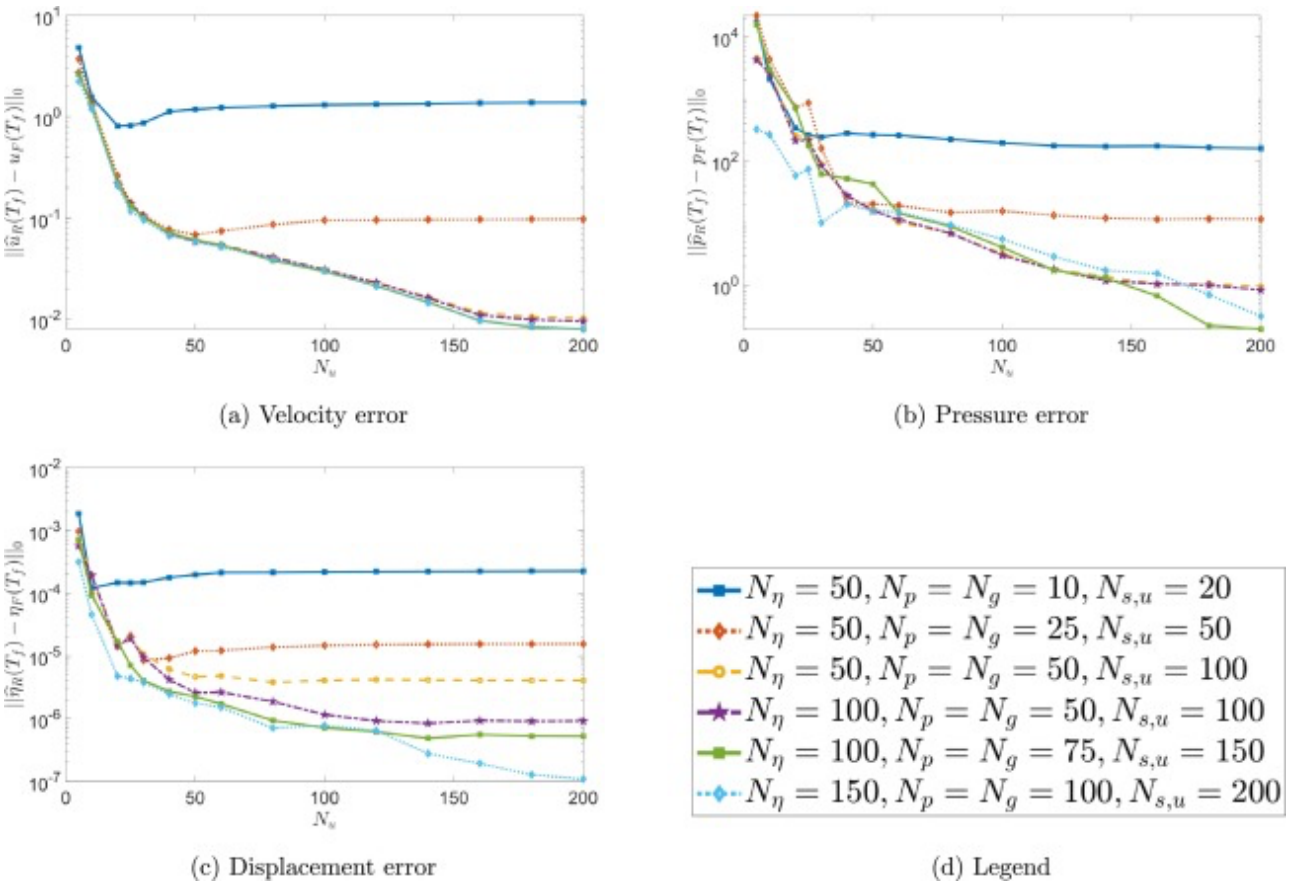

(a) Velocity error (b) Pressure error

(c) Displacement error (d) Legend

Download: Download high-res image (432KB)

Download: Download full-size image

Fig. 15. L^2 errors with respect to N_u for the parametric blood flow problem.

7. Conclusions

We have extended the Schur complement technique for full order FSI problems developed in [16] to a more flexible formulation for coupling a projection-based ROM to another ROM or to a FEM. This extension required us to utilize supremizers, and our numerical results show the necessity

of using supremizers to enrich the reduced velocity space. However, we have observed that supremizers in the reduced displacement space do not provide any additional benefit. In each of our two numerical tests, we examined the dependence of errors on various basis sizes as well as the relationship between the velocity POD basis size and the supremizer basis size. Overall, our ROM-ROM and FEM-ROM coupled formulations produce results that agree well with the FEM-FEM solution in a shorter computational time and with a large reduction in the overall system's size. The “optimal” basis sizes are problem dependent; the manufactured solution performs best with a smaller pressure basis, while the blood flow problem requires a larger pressure basis to reach the lowest errors, for example. These results are promising for solving more challenging FSI problems, as we have also observed numerically that the Schur complement matrix is still well-conditioned in the ROM-ROM case. For the numerical example presented here, we observed that FEM-ROM coupling did not provide additional accuracy as compared to the ROM-ROM model; however this is likely problem dependent and a FEM-ROM model may prove useful in problems where the ROM is unable to accurately capture the dynamics of the subdomain.

Future directions for research include extending this Schur complement partitioned method to FSI problems involving the Navier-Stokes equations on a moving domain, which will require the use of hyperreduction to deal with the nonlinearity. This method also may be applied to different FSI systems, such as the Stokes-Biot model for coupling a fluid to a poroelastic structure. Additional attention could be given to using ROMs in the predictive regime instead of solely reproductive results, including a deeper examination into the use of ROMs for parametric problems.

CRediT authorship contribution statement

Amy de Castro: Conceptualization, Methodology, Software, Visualization, Writing – original draft, Writing – review & editing. **Hyesuk Lee:** Conceptualization, Funding acquisition, Methodology, Project administration, Supervision, Writing – review & editing. **Margaret M. Wiecek:** Supervision, Writing – review & editing.

Declaration of Competing Interest

The authors declare the following financial interests/personal relationships which may be considered as potential competing interests: Hyesuk Lee reports financial support was provided by National Science Foundation under grant number DMS-2207971. Amy de Castro reports financial support was provided by National Science Foundation under grant number

DMS-2207971. If there are other authors, they declare that they have no known competing financial interests or personal relationships that could have appeared to influence the work reported in this paper.

Recommended articles

Data availability

Data will be made available on request.

References

[1] I. Akhtar, A. Nayfeh, C. Ribbens
On the stability and extension of reduced–order Galerkin models in incompressible flows: a numerical study of vortex shedding
Theor. Comput. Fluid Dyn., 23 (2009), pp. 213-237
View at publisher ↗ Crossref ↗ View in Scopus ↗ Google Scholar ↗

[2] S. Ali, F. Ballarin, G. Rozza
Stabilized reduced basis methods for parametrized steady Stokes and Navier–Stokes equations
Comput. Math. Appl., 80 (2020), pp. 2399-2416
View PDF View article View in Scopus ↗ Google Scholar ↗

[3] S. Ali, F. Ballarin, G. Rozza
Reduced basis stabilization for the unsteady Stokes and Navier–Stokes equations
arXiv preprint
arXiv:2103.03553 ↗ (2021)
Google Scholar ↗

[4] M. Astorino, C. Grandmont
Convergence analysis of a projection semi–implicit coupling scheme for fluid–structure interaction problems
Numer. Math., 116 (4) (2010), pp. 721-767
View at publisher ↗ Crossref ↗ View in Scopus ↗ Google Scholar ↗

[5] F. Ballarin, A. Manzoni, A. Quarteroni, G. Rozza

Supremizer stabilization of POD–Galerkin approximation of parametrized steady incompressible Navier–Stokes equations

Int. J. Numer. Methods Eng., 102 (2015), pp. 1136-1161

View at publisher ↗ Crossref ↗ View in Scopus ↗ Google Scholar ↗

[6] F. Ballarin, G. Rozza

POD–Galerkin monolithic reduced order models for parametrized fluid–structure interaction problems

Int. J. Numer. Methods Fluids, 82 (2016), pp. 1010-1034

View at publisher ↗ Crossref ↗ View in Scopus ↗ Google Scholar ↗

[7] F. Ballarin, G. Rozza, Y. Maday

Reduced-order semi-implicit schemes for fluid-structure interaction problems

P. Benner, M. Ohlberger, A. Patera, G. Rozza, K. Urban (Eds.), Model Reduction of Parameterized Systems, Springer, Cham (2017), pp. 149-167

View at publisher ↗ Crossref ↗ View in Scopus ↗ Google Scholar ↗

[8] G. Berkooz, P. Holmes, J.L. Lumley

The proper orthogonal decomposition in the analysis of turbulent flows

Annu. Rev. Fluid Mech., 25 (1993), pp. 539-575

View at publisher ↗ Crossref ↗ View in Scopus ↗ Google Scholar ↗

[9] J. Burkardt, M. Gunzburger, H-C. Lee

POD and CVT-based reduced-order modeling of Navier–Stokes flows

Comput. Methods Appl. Mech. Eng., 196 (2006), pp. 337-355

View PDF View article View in Scopus ↗ Google Scholar ↗

[10] E. Burman, R. Durst, M. Fernández, J. Guzmán

Fully discrete loosely coupled Robin–Robin scheme for incompressible fluid–structure interaction: stability and error analysis

Numer. Math., 151 (4) (2022), pp. 807-840

View at publisher ↗ Crossref ↗ View in Scopus ↗ Google Scholar ↗

[11] A. Caiazzo, T. Iliescu, V. John, S. Schyschlowa

A numerical investigation of velocity–pressure reduced order models for incompressible flows

J. Comput. Phys., 259 (2014), pp. 598-616

View PDF View article View in Scopus ↗ Google Scholar ↗

[12] A. Chorin
Numerical solution of the Navier-Stokes equations
Math. Comput., 22 (1968), pp. 745-762
View in Scopus ↗ Google Scholar ↗

[13] C. Colciago, S. Deparis
Reduced numerical approximation of reduced fluid-structure interaction problems with applications in hemodynamics
Front. Appl. Math. Stat., 4 (2018)
Google Scholar ↗

[14] A. de Castro, P. Bochev, P. Kuberry, I. Tezaur
Explicit synchronous partitioned scheme for coupled reduced order models based on composite reduced bases
Comput. Methods Appl. Mech. Eng. (2023), Article 116398
View PDF View article View in Scopus ↗ Google Scholar ↗

[15] A. de Castro, P. Kuberry, I. Tezaur, P. Bochev
A novel partitioned approach for reduced order model – finite element model (ROM-FEM) and ROM-ROM coupling
Earth and Space 2022 (2022), pp. 475-489
Google Scholar ↗

[16] A. de Castro, H. Lee, M.M. Wiecek
Formulation and analysis of a Schur complement method for fluid-structure interaction
arXiv:2304.15001v1 ↗ (2023)
Google Scholar ↗

[17] E. Dowell, K. Hall
Modeling of fluid-structure interaction
Annu. Rev. Fluid Mech., 33 (2001), pp. 445-490
Crossref ↗ View in Scopus ↗ Google Scholar ↗

[18] H. Fischer, A. Fau, T. Wick
Reduced–order modeling for parametrized time–dependent Navier–Stokes

equations

PAMM (2022)

Google Scholar ↗

[19] B. Galletti, C.H. Bruneau, L. Zannetti, A. Iollo

Low-order modelling of laminar flow regimes past a confined square cylinder

J. Fluid Mech., 503 (2004), pp. 161-170

View in Scopus ↗ Google Scholar ↗

[20] J.-L. Guermond, P. Minev, J. Shen

An overview of projection methods for incompressible flows

Comput. Methods Appl. Mech. Eng., 195 (2006), pp. 6011-6045

View PDF View article View in Scopus ↗ Google Scholar ↗

[21] J.-L. Guermond, L. Quartapelle

On the approximation of the unsteady Navier–Stokes equations by finite element projection methods

Numer. Math., 80 (1998), pp. 207-238

View in Scopus ↗ Google Scholar ↗

[22] M. Gunzburger, J. Peterson, J. Shadid

Reduced–order modeling of time-dependent PDEs with multiple parameters in the boundary data

Comput. Methods Appl. Mech. Eng., 196 (2007), pp. 1030-1047

View PDF View article View in Scopus ↗ Google Scholar ↗

[23] P. Holmes, J.L. Lumley, G. Berkooz

Turbulence, Coherent Structures, Dynamical Systems and Symmetry

Cambridge University Press (1996)

Google Scholar ↗

[24] A. Iollo, S. Lanteri, J-A. Désidéri

Stability properties of POD–Galerkin approximations for the compressible Navier–Stokes equations

Theor. Comput. Fluid Dyn., 13 (6) (2000), pp. 377-396

View in Scopus ↗ Google Scholar ↗

[25] A. Ivagnes, G. Stabile, A. Mola, T. Iliescu, G. Rozza

Pressure data–driven variational multiscale reduced order models

J. Comput. Phys., 476 (2023)

Google Scholar ↗

[26] I. Kalashnikova, M.F. Barone, M.R. Brake

A stable Galerkin reduced order model for coupled fluid–structure interaction problems

Int. J. Numer. Methods Eng., 95 (2013), pp. 121-144

Crossref ↗ View in Scopus ↗ Google Scholar ↗

[27] E. Karatzas, M. Nonino, F. Ballarin, G. Rozza

A reduced order cut finite element method for geometrically parametrized steady and unsteady Navier–Stokes problems

Comput. Math. Appl., 116 (2022), pp. 140-160

View PDF View article View in Scopus ↗ Google Scholar ↗

[28] K. Kean, M. Schneier

Error analysis of supremizer pressure recovery for POD based reduced-order models of the time–dependent Navier–Stokes equations

SIAM J. Numer. Anal., 58 (4) (2020), pp. 2235-2264

Crossref ↗ View in Scopus ↗ Google Scholar ↗

[29] P. Kuberry, H. Lee

A decoupling algorithm for fluid-structure interaction problems based on optimization

Comput. Methods Appl. Mech. Eng., 267 (2013), pp. 594-605

View PDF View article View in Scopus ↗ Google Scholar ↗

[30] T. Lassila, A. Manzoni, A. Quarteroni, G. Rozza

A reduced computational and geometrical framework for inverse problems in hemodynamics

Int. J. Numer. Methods Biomed. Eng., 29 (2013), pp. 741-776

Crossref ↗ View in Scopus ↗ Google Scholar ↗

[31] T. Lassila, A. Manzoni, A. Quarteroni, G. Rozza

Model order reduction in fluid dynamics: challenges and perspectives

A. Quarteroni, G. Rozza (Eds.), Reduced Order Methods for Modeling and Computational Reduction,

Springer (2014), pp. 235-273

Crossref ↗ Google Scholar ↗

[32] T. Lassila, A. Quarteroni, G. Rozza

A reduced basis model with parametric coupling for fluid–structure interaction problems

SIAM J. Sci. Comput., 34 (2012), pp. A1187-A1213

Crossref ↗ View in Scopus ↗ Google Scholar ↗

[33] S-H. Lee, Y. Kim, D. Gong, *et al.*

Fast and novel computational methods for multi-scale and multi-physics: FETI and POD-ROM

Multiscale Sci. Eng., 2 (2020), pp. 189-197

Google Scholar ↗

[34] X. Li, Y. Luo, M. Feng

An efficient Chorin–Temam projection proper orthogonal decomposition based reduced-order model for nonstationary Stokes equations

J. Sci. Comput., 93 (2022), p. 64

View PDF View article Google Scholar ↗

[35] E. Liberge, A. Hamdouni

Reduced order modelling method via proper orthogonal decomposition POD for flow around an oscillating cylinder

J. Fluids Struct., 26 (2010), pp. 292-311

View PDF View article View in Scopus ↗ Google Scholar ↗

[36] T. Lieu, C. Farhat, M. Lesoinne

Reduced-order fluid/structure modeling of a complete aircraft

Comput. Methods Appl. Mech. Eng., 195 (2006), pp. 5730-5742

View PDF View article View in Scopus ↗ Google Scholar ↗

[37] J. Lumley

The structure of inhomogeneous turbulent flows

Atmospheric Turbulence and Radio Wave Propagation (1967), pp. 166-178

View in Scopus ↗ Google Scholar ↗

[38] A. Manzoni

Reduced models for optimal control, shape optimization and inverse problems in haemodynamics

Technical report, EPFL

(2012)

Google Scholar ↗

[39] B. Noack, P. Papas, P. Monkewitz

The need for a pressure–term representation in empirical Galerkin models of incompressible shear flows

J. Fluid Mech., 523 (2005), pp. 339-365

Crossref ↗ View in Scopus ↗ Google Scholar ↗

[40] M. Nonino, F. Ballarin, G. Rozza

A monolithic and a partitioned, reduced basis method for fluid–structure interaction problems

Fluids, 6 (2021), pp. 229-263

Crossref ↗ View in Scopus ↗ Google Scholar ↗

[41] M. Nonino, F. Ballarin, G. Rozza, Y. Maday

Projection based semi-implicit partitioned reduced basis method for fluid-structure interaction problems

J. Sci. Comput., 94 (1) (2023), p. 4

View in Scopus ↗ Google Scholar ↗

[42] M. Nonino, F. Ballarin, G. Rozza, Y. Maday

A reduced basis method by means of transport maps for a fluid–structure interaction problem with slowly decaying Kolmogorov n–width

Adv. Comput. Sci. Eng., 1 (2023)

Google Scholar ↗

[43] K. Peterson, P. Bochev, P. Kuberry

Explicit synchronous partitioned algorithms for interface problems based on Lagrange multipliers

Comput. Math. Appl., 78 (2019), pp. 459-482

View PDF View article View in Scopus ↗ Google Scholar ↗

[44] I. Prusak, D. Torlo, M. Nonino, G. Rozza

Optimisation–based coupling of finite element model and reduced order model for computational fluid dynamics

arXiv preprint

arXiv:2402.10570 ↗ (2024)

Google Scholar ↗

[45] A. Quarteroni, A. Manzoni, F. Negri

Reduced Basis Methods for Partial Differential Equations: an Introduction, vol. 92

Springer (2015)

Google Scholar ↗

[46] C. Rowley, T. Colonius, R. Murray

Model reduction for compressible flows using POD and Galerkin projection

Phys. D, Nonlinear Phenom., 189 (1–2) (2004), pp. 115-129

View PDF View article View in Scopus ↗ Google Scholar ↗

[47] G. Rozza, D.B.P. Huynh, A. Manzoni

Reduced basis approximation and a posteriori error estimation for Stokes flows in parametrized geometries: roles of the inf–sup stability constants

Numer. Math., 125 (2013), pp. 115-152

Crossref ↗ View in Scopus ↗ Google Scholar ↗

[48] G. Rozza, K. Veroy

On the stability of the reduced basis method for Stokes equations in parametrized domains

Comput. Methods Appl. Mech. Eng., 196 (2007), pp. 1244-1260

View PDF View article View in Scopus ↗ Google Scholar ↗

[49] S. Rubino

Numerical analysis of a projection-based stabilized POD-ROM for incompressible flows

SIAM J. Numer. Anal., 58 (4) (2020), pp. 2019-2058

Crossref ↗ View in Scopus ↗ Google Scholar ↗

[50] L. Sirovich

Turbulence and the dynamics of coherent structures: part 1-part 3

Q. Appl. Math., 45 (1987), pp. 561-590

Crossref ↗ Google Scholar ↗

[51] K.C. Sockwell, K. Peterson, P. Kuberry, P. Bochev, N. Trask

Interface flux recovery coupling method for the ocean–atmosphere system

Results Appl. Math., 8 (2020), pp. 100-110

Google Scholar ↗

[52] G. Stabile, G. Rozza

Finite volume POD–Galerkin stabilised reduced order methods for the parametrised incompressible Navier–Stokes equations

Comput. Fluids, 173 (2018), pp. 273-284

View PDF View article View in Scopus ↗ Google Scholar ↗

[53] A. Tello, R. Codina, J. Baiges

Fluid structure interaction by means of variational multiscale reduced order models

Int. J. Numer. Methods Eng., 121 (2020), pp. 2601-2625

Crossref ↗ View in Scopus ↗ Google Scholar ↗

[54] R. Temam

Une méthode d'approximation de la solution des équations de Navier-Stokes

Bull. Soc. Math. Fr., 96 (1968), pp. 115-152

Crossref ↗ Google Scholar ↗

[55] W. Wang, Y. Yan

Strongly coupling of partitioned fluid–solid interaction solvers using reduced-order models

Appl. Math. Model., 34 (2010), pp. 3817-3830

View PDF View article View in Scopus ↗ Google Scholar ↗

Cited by (0)

1 Partially supported by the National Science Foundation under grant number DMS-2207971.

2 Partially supported by the National Science Foundation under grant number DMS-2207971.

View Abstract